“*In-Plane*” site-specific FIB lamella extraction from deformed magnetite and the investigation of low angle grain boundaries under TEM

Manish A. Mamtani[1], Olivia Wenzel[2], Agnes Kontny[3], Christoph Hilgers[3], Erich Müller[2], A.R. Renjith[4], Maria-Gema Llorens[5], Enrique Gomez-Rivas[6]

[1] Department of Geology and Geophysics, Indian Institute of Technology, Kharagpur-721302, India.

[2] Laboratory for Electron Microscopy, Karlsruhe Institute of Technology, Engesserstrasse-7, Build. 30.22 (Physik Flachbau), 76131 Karlsruhe, Germany.

[3] Institute of Applied Geosciences (Structural Geology & Tectonics), Karlsruhe Institute of Technology, Adenauerring 20a, 76131 Karlsruhe, Germany.

[4] Nano-Analysis division, Oxford Instruments India Pvt Ltd., Plot No.A-279, Ground Floor, Road No.16A, Ambica Nagar, Wagle Industrial Estate, Thane (West)-400604, India.

[5] Geosciences Barcelona (GEO3BCN-CSIC). Carrer de Lluís Solé i Sabarís s/n, 08028, Barcelona, Spain.

[6] Departament de Mineralogia, Petrologia i Geologia Aplicada. Facultat de Ciències de la Terra, Universitat de Barcelona, Martí i Franquès s/n. 08028 Barcelona, Spain.

This is a post-print version of the article published in:

Journal of Structural Geology 174 (2023) 104937.

DOI: https://doi.org/10.1016/j.jsg.2023.104937

"*In-Plane*" site-specific FIB lamella extraction from deformed magnetite and the investigation of low angle grain boundaries under TEM

Manish A. Mamtani[1], Olivia Wenzel[2], Agnes Kontny[3], Christoph Hilgers[3], Erich Müller[2], A.R. Renjith[4], Maria-Gema Llorens[5], Enrique Gomez-Rivas[6]

[1] Department of Geology and Geophysics, Indian Institute of Technology, Kharagpur-721302, India.

[2] Laboratory for Electron Microscopy, Karlsruhe Institute of Technology, Engesserstrasse-7, Build. 30.22 (Physik Flachbau), 76131 Karlsruhe, Germany.

[3] Institute of Applied Geosciences (Structural Geology & Tectonics), Karlsruhe Institute of Technology, Adenauerring 20a, 76131 Karlsruhe, Germany.

[4] Nano-Analysis division, Oxford Instruments India Pvt Ltd., Plot No.A-279, Ground Floor, Road No.16A, Ambica Nagar, Wagle Industrial Estate, Thane (West)-400604, India.

[5] Geosciences Barcelona (GEO3BCN-CSIC). Carrer de Lluís Solé i Sabarís s/n, 08028, Barcelona, Spain.

[6] Departament de Mineralogia, Petrologia i Geologia Aplicada. Facultat de Ciències de la Terra, Universitat de Barcelona, Martí i Franquès s/n. 08028 Barcelona, Spain.

Abstract

In this study a *modus operandi* to investigate site-specific nanostructures in thin films (lamellae) excavated "*in-plane*" across (sub)grain boundaries is presented. This is done by discussing the case of a magnetite grain hosted in a thin section of banded iron formation (Norway) that is prepared parallel to the kinematic reference frame (XZ section of the strain ellipsoid). SEM-EBSD analysis reveal that the magnetite grains do not develop a strong crystallographic preferred orientation, although individual grains are strained and show evidence of intracrystalline deformation in form of low angle grain boundaries (LAGB's). Two "*in-plane*" lamellae using focused ion beam (FIB) technique are excavated from a magnetite grain in the kinematic reference frame, and nanostructures are studied along three LAGB's using high resolution transmission electron microscopy imaging followed by Fourier transformation (FT), inverse FT and estimation of dislocation densities. Our data establish an empirical relationship for the studied LAGBs, namely, the smaller the angle between LAGB and X-direction, the larger are the shear strain and dislocation density. This relationship is validated from numerical simulations of viscoplastic deformation and dynamic recrystallisation of polycrystalline aggregates of halite, which is also a cubic mineral analogous to magnetite. In addition to the site-specific "*in-plane*" FIB lamella information, this study also shows that in a deformed mineral the different orientations of the LAGB compared to the principal strain axes show a different dislocation density. This approach of full tracking of the extension direction (X) from the macroscopic to the nano-scale could play an important role in forward modelling of microstructure evolution in future studies.

Keywords: FIB lamella; TEM; magnetite; nanostructures; low angle grain boundary; numerical simulation, dislocation density

1. Introduction

Microstructural studies are commonly done in thin sections that are prepared parallel to the stretching lineation and perpendicular to the foliation, i.e., the XZ section of the strain ellipsoid (Simpson, 1986; Passchier et al., 1990; Passchier and Trouw, 2005). Structures in this reference frame have been critical in evaluating kinematics of deformation, from the macro- to the micro- scales (e.g., Xypolias, 2010 and references therein). In the absence of visible planar and/or linear fabric in a rock, anisotropy of magnetic susceptibility (AMS) has been effectively used to identify the kinematic reference frame and subsequently evaluate and quantify the fabric (e.g., Archanjo et al., 1995; Sen and Mamtani, 2006; Mamtani et al. 2013, 2017; Mamtani, 2014; Bella Nké et al., 2018). Lattice Preferred Orientation (LPO) studies of minerals (such as quartz, olivine etc.) have also been traditionally performed in the XZ section using instruments such as the U-stage or SEM-Electron Backscatter Diffraction (EBSD), which have enhanced our knowledge of deformation processes and slip systems that operate at the microscopic scale (e.g., Bouchez and Duval, 1982; Schmid and Casey, 1986; Mainprice and Nicolas, 1989; Law, 1990; Takeshita and Hara, 1998; Bestmann et al., 2004; Toy et al., 2008; Drury et al., 2011; Renjith et al., 2016; Mamtani et al, 2017; Renjith et al., 2016 amongst others). In order to further enhance the knowledge of deformation mechanisms, it is necessary to look at nanostructures and grain boundaries under the Transmission Electron Microscope (TEM) (e.g., Bouchez and Nicolas, 2021). Ion milling has been in vogue for preparing samples for TEM; this involves bombardment of ions on a thin wafer of rock that is mounted on a TEM mesh grid until electron transparency for TEM observations of nanostructures is achieved (e.g., Goodwin and Wenk, 1990; Trepmann and Stöckert, 2003; Viti et al., 2016). However, the limitation of this method is that it is not possible to exactly perform site-specific TEM imaging within a grain and its nanostructural analysis.

In order to study site-specific nanostructures within a mineral under TEM, thin film (lamella) must be excavated using focused ion beam (FIB) with the help of SEM (Giannuzzi and Stevie, 1999, 2005). Recently, Mamtani et al. (2020) have shown the importance of using SEM-EBSD studies in identifying low- and high- angle grain boundaries (LAGB and HAGB) within magnetite hosted in a thin section (XZ) of a mylonitized mica schist, and subsequently excavating site-specific FIB lamella from across specific grain boundaries. It is well accepted that intracrystalline deformation by dislocation creep leads to movement of dislocations, which interact to form subgrain boundaries. Subgrain boundaries with crystallographic misorientation generally $<15^{\circ}$ across them are generally considered as low-angle grain boundaries (LAGB) (Poirier, 1980); others are categorized as high-angle grain boundaries (HAGB) (also see Bouchez and Nicolas, 2021). The FIB technique allows site-specific lamella extraction across LAGB and HAGB within a large grain that was identified from SEM-EBSD data. Mamtani et al. (2020) were able to document differences in the nanostructures at LAGB and HAGB using this *modus operandi*. However, FIB lamellae are conventionally excavated perpendicular to the plane of observation, and are thus cross-sections (Giannuzzi and Stevie, 1999, 2005; Langford and Petford-Long, 2001; Kruhl et al., 2013). Whilst rock thin sections used for microstructural analyses are commonly made along the XZ plane, FIB lamellae excavated are perpendicular to it; this was also the case for the study of Mamtani et al. (2020). As a consequence, the plane of observation of a rock thin section under the light microscope and SEM is different from the plane of observation of a FIB lamella (excavated from the thin section) under TEM. Therefore, the orientation of the sub-grain boundaries and the nanostructures observed under TEM cannot be unequivocally related to the kinematic reference frame, and hence limits the interpretation of nanoscale observations. To overcome this limitation, it is necessary to prepare site-specific in-plane FIB lamella that is excavated parallel to the XZ thin section, wherein the X direction can be traced on the plane of observation (i.e., XZ) from the hand-specimen, through the thin section (light microscope) and the FIB lamella (SEM and TEM). This procedure can open up whole new sets of possibilities to structural geologists that can help relate kinematic observations at the nanoscale to larger scale kinematics and also address some fundamental questions such as – (a) how is the orientation of a (sub)grain boundary (LAGB/HAGB) related to shear strain and dislocation density? (b) Is there any difference in nanostructures developed along grain boundaries that are oriented at different angles to the inferred extension direction of strain in a rock sample? Answers to these questions are intricately related to topics in materials sciences where it is known that nanostructures at grain boundaries influence their mechanical properties (strength/rheology) and in experiments the spatial geometry of grain boundaries vis-à-vis loading direction has also been reported to play a critical role in slip transmission and dislocation motion (e.g., Johannesson and Thölén, 1970; Hirth, 1972; Johnson et al., 2004; Ferreira et al., 2010; Liu et al., 2012; Kheradmand et al., 2016; de Almeida Ribeiro and de Koning, 2021;).

Despite the above listed usefulness of performing TEM studies on site-specific in-plane FIB lamella, there are only a few studies focused on this, primarily because of the challenges involved in extracting thin films parallel to the plane of observation. Li et al. (2018) were the first to present a step-wise *modus operandi* to extract such lamella (from polycrystalline spinel). Since their objective was to develop and present a detailed methodology, Li et al (2018) did not discuss the possible application of TEM investigations in such lamella vis-à-vis strain. In an earlier study Kogure et al. (2014) investigated subgrain boundaries around *b*-axis of deformed orthopyroxene (Opx) in "plan-view specimens" of a mylonite (Hidaka Metamorphic Belt, Japan) that was prepared by a combination of chemical etching, EBSD and FIB. They identified *b*-axis orientation of Opx crystals and mounted the excavated lamella on the TEM copper grid either orthogonally or at an inclination to ensure that the TEM incident beam is parallel to the *b*-axis. Although this work (Kogure et al., 2014) related the TEM images with *b*-axis orientation, it (i) did not track the X direction in the various images and (ii) did not provide the reader with the detailed steps of sample preparation to replicate the study subsequently. More recently, Igami and Michibayashi (2021) performed an integrated SEM-Transmission Kikuchi Diffraction (TKD) and TEM investigation of ultramylonite peridotite on a XZ section. However, the extension direction (X) was not explicitly marked in the images (except in one EBSD map, Fig. 5 of Igmai and Michibayashi, 2021), as a consequence of which, the TEM results cannot be unequivocally related to the extension direction even if the images are within the kinematic reference frame. It is also important to note that the work of Li et al (2018) was not referred by Igami and Michibayashi (2021) implying that some different methodology was adopted, which is not described in their work. It is unclear to the reader if the XZ section was excavated in-plane (i.e., parallel to XZ plane) like Li et al (2018), or if the XZ section was obtained by excavating a cross-section perpendicular to YZ plane.

This detailed description thus brings to light that there is no investigation in geoscience literature, where the reader can relate structures from the hand-specimen (macro-/meso- scale) through microscopic scale (light microscope and SEM) to the nano-scale (TEM) keeping full track of the extension direction (X) in the kinematic reference frame. This would have the advantages to address several questions listed in (a) and (b) (above), and the present paper fills this lacuna. We present an exhaustive account of excavating site-specific in-plane FIB lamella from the kinematic reference frame that can be replicated by any geoscientist without any confusion, and keeping a complete track of the X direction at all scales of observation. Eventually, we discuss implications of such studies in enhancing our understanding of nanoscale processes at (sub)grain boundaries and modelling microstructure evolution. Due to our experience of dealing with SEM and TEM data from magnetite (Mamtani et al., 2020), in this study, we have investigated grain boundaries in magnetite. But, we advocate that this approach can be adopted for any mineral and can form the basis of considerable future research on "*nanotectonics*" in naturally deformed rocks.

2. Sample description and determination of the kinematic reference frame

The material used for this SEM-EBSD and TEM study is a metamorphic quartz-magnetite banded iron ore from the Sydvaranger mine (Finnmark, Norway). According to Bugge (1980), the BIFs of the Sydvaranger mine are Archaean in age (older than 2,500 Ma). Regional geological descriptions are published in Bugge (1980), Bjørlykke et al. (1985) and Boyd et al. (2016), amongst others. Our sample comes from a hand specimen shown in Fig. 1a. It comprises alternating dark (magnetite-rich) and light (quartz-rich) bands. Earlier studies have established that magnetite is pure and stoichiometric (Reznik et al., 2016). The banding in these rocks defines the foliation plane and is considered to be parallel to the XY plane of the strain ellipsoid with X>Y>Z defining the three principal axes of the strain ellipsoid (Hobbs, Means and Williams, 1976). It is noted that our first requirement was to prepare a rock thin section parallel to the kinematic reference frame, i.e., XZ section of the strain ellipsoid. Since the rock lacked any visible stretching lineation, we used anisotropy of magnetic susceptibility (AMS) to characterize the fabric geometry. AMS involves placing a sample (cylindrical or cubic) in an external magnetic field in different orientations and measuring the induced magnetization in each orientation. The magnetic induction takes place along the "*easy*" axis (crystallographic or shape) of the different minerals present in the sample (Tarling and Hrouda, 1993). Therefore, rocks with randomly oriented minerals are magnetically isotropic since they have the same magnetic susceptibility in different orientations. However, deformed rocks have a preferred orientation of minerals and hence possess an AMS. This helps identify the fabric in a rock, even if the visible foliation and/or lineation is not well-developed. AMS is represented as a magnetic susceptibility ellipsoid, a second-order tensor with three principal axes, $K_1>K_2>K_3$. The K_1K_2 plane is the magnetic foliation, while K_1 is the magnetic lineation; the reader is referred to Tarling and Hrouda (1993) for details about AMS and formulae of various parameters. For the present study, it is important to note that the orientations of principal axes of the AMS ellipsoid ($K_1>K_2>K_3$) have been equated with those of the strain ellipsoid (X>Y>Z) as reported in several past studies (Tarling and Hrouda, 1993; Borradaile and Henry, 1997; Sen and Mamtani, 2006; Borradaile and Jackson, 2010; Mamtani et al., 2013). The magnetic foliation (K_1K_2 plane) is parallel to the visible foliation (XY), and the magnetic lineation (K_1) defines the X direction of the strain ellipsoid. Hence, the K_1K_3 section of the AMS ellipsoid is equated with XZ of the strain ellipsoid, which makes AMS a very useful tool in the identification of the kinematic reference frame for petrofabric studies (e.g., Archanjo et al., 1995; Renjith et al., 2016; Mamtani, 2014, 2022; Bella Nké et al., 2018; Goswami et al., 2018; Mamtani et al., 2017, 2021). We measured AMS of a BIF cube (2 cm x 2 cm x 2 cm dimension; Fig. 1b,c) with the KLY-4S Kappabridge (AGICO, Czech Republic) housed in the magnetic laboratory of the Institute of Applied Geosciences, KIT Karlsruhe (Germany). Figures 1b, c document that the magnetic foliation (K_1K_2 plane) is vertical, in agreement with the banding, and the magnetic lineation (K_1) is horizontal; this helps mark the mineral stretching direction on the foliation (banding).

In order to further ascertain that this correlation between the three principal axes of the AMS and strain ellipsoids is true, we prepared a rock thin section parallel to the K_1K_3 plane of the AMS ellipsoid (Fig. 1d) and performed SEM-based EBSD analysis of quartz (Fig. 2a-c; see Appendix-1 for details about instrument and analytical conditions). The quartz CPO (Fig. 2c) is comparable to standard pole figures recorded in XZ reference frame under dextral shearing with basal<a> and rhomb<a> being the dominant slip systems typical of rocks deformed below 500^{o}C temperature (e.g., Schmid and Casey, 1983; Law, 1986; Passchier and Trouw, 2005). Thus, with regards to the sample geometry and reference frame of the BIF specimen, we conclude that (a) the three principal axes of the AMS ellipsoid ($K_1>K_2>K_3$) represent the respective principal axes of the strain ellipsoid (X>Y>Z), and (b) the rock thin section prepared parallel to the K_1K_3 plane of the AMS ellipsoid (Fig. 1d, 2a) is parallel to the kinematic reference frame (XZ). It may be noted that henceforth in this paper, the frame of reference will be referred to as XZ section.

3. SEM-EBSD Analysis of Magnetite: *Identifying the Region of Interest*

Magnetite grains in the present BIF specimen are commonly inequigranular in shape and elongated parallel to the stretching direction ($X=K_1$). An inverse pole figure (IPF) map from SEM-EBSD analysis of magnetite confirms this (Fig. 2d) and also reveals that the magnetite grains have an elongated shape parallel to several quartz grains; this also implies that the mineral phases were subjected to the same strain. The lower hemisphere equal area projection of {100}, {110} and {111} axes of all magnetite grains analysed is presented as supplementary data-1. This reveals that there is considerable variation in the crystallographic axes orientations of magnetite. The IPF map (Fig. 2d) helped identify large magnetite grains with high aspect ratio as well as with variations in crystallographic orientations. The magnetite grain in the centre of Fig. 2d (demarcated by arrow) was selected for detailed SEM and EBSD analysis; this magnetite grain is also marked by an arrow and a box in Fig. 2a and 2b, respectively. This particular magnetite grain is elongated parallel to the X-direction, has a long-axis dimension of 235 μm, and also shows considerable variation in magnetite CPO, which is evident from the IPF map (Fig. 2e). No microstructural evidence of asymmetric pressure shadows or development of strain fringes in contact with the magnetite grains that can be related to rotation of magnetite are noted (e.g., Mamtani et al., 2011). Forescatter detector (FSD) image of this magnetite shows the presence of microcracks, but with some parts of the grain having significant orientation contrast (areas marked by arrows in Fig. 2f); this implies intracrystalline deformation. The IPF map of the magnetite (Fig. 3a) supports the latter.

We also used the EBSD data to prepare kernel average misorientation (KAM) map of the selected magnetite grain (Fig. 3b). This allows to map areas of local high misorientation within the magnetite. It maybe noted that the local misorientation represented by KAM maps is well-correlated with local microscale deformation (plastic strain) and geometrically necessary dislocations (Brewer et al., 2009; Wheeler et al., 2009; Kamaya, 2011; Moussa et al., 2015). The IPF and KAM maps (Figs. 3a,b) were useful to select the profile line UV along which crystallographic misorientation was measured (Fig. 3c). Misorientations of ca ≤6° are recorded in proximity to the point U up to a distance of ca 40 μm along the profile line (Fig. 3c). This is the region of the magnetite grain that also has significant orientation contrast (Fig. 2f), shows subgrains and evidence of strain (Fig. 3a,b), and is devoid of microcracks (Fig. 3d). Thus, the misorientations can be confidently inferred to be on account of intracrystalline deformation, and this part of the magnetite grain is recognized as the region of interest (marked ROI in Fig. 3c,d). It comprises low-angle grain boundaries (LAGB's) (Fig. 3c). Beyond the region of interest, in the central part of the misorientation profile (UV), several high angles of misorientation (>20° to as high as 44°) are recognized (Fig. 3c). Careful imaging of these areas under the SEM revealed the presence of microcracks (black arrows in Fig. 3d). Hence, the central part of the misorientation profile (UV) with high misorientation angles is classified as a region of microcracks (marked ROM in Fig. 3c). High-angle grain boundaries (HAGB's) are known to be important sites for development of microcracks in various materials (e.g., Sangid et al., 2011). Therefore, there maybe a contribution of such cracking (brittle deformation) in the high misorientation angles recorded in the area marked ROM in Figs. 3c,d; also see Mamtani et al., 2011). Since our focus is on intracrystalline deformation, we restrict our TEM investigation to LAGB's within the region of interest (marked ROI in Fig. 3d).

4. Methods

4.1. "In-Plane" magnetite lamella extraction containing LAGB using FIB – modus operandi

The rock thin-section of the BIF sample is a XZ section, and hence the ROI lies within this XZ plane. The quartz CPO has already been used to infer that the sense of shear is dextral (Fig. 2c). Our objective in this study is to investigate the nanostructures under TEM in the same reference frame as that of the rock thin section. To meet this objective it was important to excavate site-specific thin-film/lamella for TEM investigation parallel to the XZ plane. The block diagram of Fig. 4a-i provides a 3D perspective of the sample reference frame and the

ROI (dashed box) in the XZ plane (Fig. 4a-ii). The inset in Fig. 4a-iii shows the exact part of the ROI that contains the LAGB's identified based on the misorientation profile (compare with Fig. 3a,b).

We adopted the *in-situ* lift-out (INLO) lamella extraction technique using FIB to excavate lamellae L1 and L2 (e.g., Heaney et al., 2001; Giannuzzi and Stevie, 2005; Mayer et al., 2007). This method involves cutting and extracting the lamella and transferring it to a TEM grid, where thinning to electron transparency is performed using an internal tungsten nanomanipulator needle inside the FIB chamber. In order to excavate the magnetite lamella parallel to the plane of view (XZ) from the thin section, we adopted a protocol similar to Li et al. (2018) for "*in-plane*" sample preparation using FIB. The rock thin section was mounted on the bulk stage of the FIB milling station FEI DualBeam Strata 400S with a gallium (Ga^+) source housed in the Laboratory for Electron Microscopy (LEM) of Karlsruhe Institute of Technology (Karlsruhe, Germany). The stage (with the thin section) was tilted 52° and four platinum (Pt) straps were first deposited on the LAGB's in the identified ROI (labelled L1, L2, bk1, bk2 in Fig. 4a-iii). L1 and L2 were the principal targeted areas for lamella extraction. Pt straps bk1 and bk2 also lay, respectively, on the LAGB's. These were deposited as a back-up for the study if a problem is encountered in the FIB lamella preparation with L1 and/or L2. Additional Pt bars (1 μm thick) were deposited on the four sides of each strap (L1 and L2). The excavation was done in the tilted position from all the sides using 30 kV/6.5 nA gallium ion beam, but ensuring to leave a "bridge" at one of the short edges of the lamella being excavated; this supports the lamella until it is cut free from the thin section. The procedure involved tilting the sample back to 0° and undercutting a wedge from below the surface of the lamella, and then attaching (glueing) the top to tungsten manipulator needle with Pt, before lifting it from the thin section (see Li et al., 2018 for a step-wise description of the technique to extract "*in-plane*" lamella). This ensured that the INLO of the FIB lamella was done parallel to the XZ section. This step of the INLO for magnetite lamella L1 and L2 is shown in Fig. 4b-i and 4b-ii, respectively; fig. 4b-iii shows the ROI in the thin section that remains after the excavation of two "*in-plane*" lamellae (L1 and L2). Each excavated lamella was mounted on an individual FIB Lift-Out TEM grid (Copper, 2 posts) placed on the flip-stage of the instrument and further thinned to ~50 nm using a 30 kV, 2.7 nA gallium beam for the rough milling and 26 pA for final thinning. As a final step, the sample was polished and cleaned with a 5 kV (71 pA ion current) to remove any damaged layers that the high energy ion beam may have induced.

As shown in Fig. 4b-i, ii, during the INLO of lamellae, the tungsten manipulator needle (marked TN in Fig. 4b) was attached (glued) to the bottom left of each lamella using Pt from the FIB. We ensured that some Pt from the glueing remains at this spot after detachment (marked as *M* at bottom left of lamella in Fig. 4b-i, ii). This acts as a "*marker*" to recognize the exact orientation of the lamella under TEM. Care was taken to mount the copper grid (containing the lamella) on the TEM specimen holder with top surface being the top of the plan view within the XZ reference frame. In this position, the glueing Pt that was intentionally left over at the point of detachment as a marker "*M*" lies at the bottom left of the lamella. This ensures that the nanostructures observed under TEM can be related to the kinematic reference frame.

4.2. TEM investigation of LAGB's in magnetite "in-plane" FIB lamella

Nanostructures in each "*in-plane*" FIB lamella excavated from the XZ reference frame of the thin section were studied using a Philips CM 200 FEG/ST TEM (LEM, KIT Karlsruhe, Germany) operated at 200 kV. TEM observations were made using bright field (BF-) and dark field (DF-) imaging conditions (Williams and Carter, 2009). The crystal orientation was determined by selected area electron diffraction (SAED; selected area aperture of 100 μm at a selected area size of ≥ 300 nm) and high-resolution TEM (HRTEM). The HRTEM images were analysed by two-dimensional (2D) Fourier transformation (FT) performed with ImageJ (Scheider et al., 2012), which were compared with calculated diffraction patterns using JEMS (Stadelmann, 1987). Further, dislocation analysis was performed on Bragg-filtered HRTEM images, where pairs of reflections were selected in the FT-image, and inverse Fourier transformed (IFT) using ImageJ. Dislocation density, ρ (=1/D^2) with the unit 1/nm^2, which is the dislocation lines that thread a unit surface area (D) was also determined from TEM data (e.g., see Ohring, 1995).

5. Results

5.1. TEM analysis of lamella L1:

Lamella L1 contains the LAGB-1. Fig. 5a is an overview SEM image of the lamella on the TEM grid showing its exact orientation in the XZ reference frame. As discussed in section 4 (above), the Pt left over after detaching the manipulator needle (arrow *M*) lies at the bottom left of the lamella, thus ensuring visualization of all the nanoscale structures in the XZ reference frame. The position of LAGB-1 in the lamella vis-à-vis thin section can be compared with the inset in Fig. 5a and Fig. 4. Fig. 5b is TEM image of the LAGB-1 taken under BF-condition with [101] zone axis, which shows the trace of the grain boundary at a magnification greater than that of Fig. 5a. It should be noted that the trace of the LAGB-1 is straight and makes a very low angle with the X direction (angle θ =4°). This low angle is also obvious in the overview image (Fig. 5a). HRTEM imaging of LAGB-1 and data processing that involved FT and IFT, including Bragg filtering, reveals presence of nano-stripes. Fig. 6a is one such HRTEM image in [114] zone axis that prominently shows nano-stripes and establishes that the trace of LAGB-1 is parallel to the [$31\bar{1}$] direction. The FT images can be indexed with Miller indices for cubic (spinel-type) Fe_3O_4 in [114] zone axis revealing that the misorientation of the crystal lattice on either side of the LAGB-1 is between 4-5° (Figs. 6b-e). Rotation angles of 4.9° (α) and 4.2° (β) are determined at $(2\bar{2}0)$ and $(1\bar{3}1)$, respectively (Fig. 6e), which leads to a double reflection. It may be noted that these angles correlate well with the ca 5° misorientation across the LAGB-1 that was determined from the EBSD misorientation profile (Fig. 3c). This implies that the vorticity axis is perpendicular to the plane of view and the lamella excavated is parallel to the vorticity profile plane; the elongated shape of the magnetite grains in the thin section, and the asymmetric distribution of quartz CPO obtained from EBSD (Fig. 2) are consistent with this inference.

Fig. 7a is a high magnification HRTEM image of a part of LAGB-1 demarcated in Fig. 6a that showed the nano-stripes (fringe-like patterns). Similar fringes have been reported at grain boundaries that are often referred to as Moiré fringes; the primary cause for the development of such fringe-like patterns is superimposition of misoriented crystal lattices associated with translation and/or rotation (e.g., Mitsuishi et al., 1951; Hillier, 1954; Fitzgerald and Mannami, 1966; McLaren, 1991; Shigematsu et al., 2006; Williams and Carter, 2009). Whilst Won et al. (2007) have related Moiré fringes at grain boundaries with strain, other studies (e.g. Shigematsu et al., 2006) have shown Moiré fringes to be associated with dislocations at quartz grain boundaries. For magnetite as well, Moiré fringes at LAGB and HAGB have been shown to be associated with several defects (dislocations, stacking faults, nano-twins); these defects were manifested by the presence of blurred contrast in HRTEM images indicating distorted atomic planes (see Figs. 6, 8 of Mamtani et al., 2020). The striped area at LAGB-1 in the present study, although not exactly like the Moiré patterns of Mamtani et al. (2020), does show domains of wavy blurred contrast (Fig. 6a, 7a). IFT along with Bragg filtering using $(\bar{2}20)$ and $(2\bar{2}0)$ for the region in Fig. 7a, reveals the presence of dislocations

(Fig. 7b), thus implying relation to deformation/strain. Dislocation density (ρ) was calculated from a Bragg filtered HRTEM image of the LAGB-1 (Fig. 6a) using ($\bar{2}20$) and ($2\bar{2}0$) (see Supplementary data-2a) as well as ($\bar{3}\bar{1}1$) and ($31\bar{1}$) (Supplementary data-2b). It is noted that ρ at the LAGB-1 is of the order of 10^{-1} dislocations/nm^2, and varies between 4.4 x 10^{-1} dislocations/nm^2 to 1.2 x 10^{-1} dislocations/nm^2 at the LAGB-1 (Supplementary data-2).

5.2. TEM analysis of lamella L2:

FIB lamella L2 was excavated from ROI, where the misorientation along the profile UV was very low (<2°; see Fig. 3c and Fig. 4a). Figs. 8a,b show lamella L2 in the same reference frame as lamella L1 (in Fig. 5a) with the Pt leftover after detaching the manipulator needle (arrow *M*) located on the bottom left. LAGB's, though faint, are recognizable in the BF-TEM image in [001] zone axis (e.g., LAGB-2 and LAGB-3 are marked by arrows in Fig. 8b). The poor contrast across the LAGB's implies (and supports) low misorientation across them. Small inclusions (marked "*I*" in Fig. 8b) are also noted along some LAGBs in this lamella (L2).

TEM images of LAGB-2 and LAGB-3 in [001] and [112] zone axis, respectively, are presented in Figs. 8c and 8d. These low magnification TEM images allow us to visualize the trace of the LAGB's in the FIB lamella (kinematic reference frame) vis-à-vis extension (X) direction. Unlike the trace of LAGB-1 (lamella L1; Fig. 5) that is straight (linear) and made a low angle with X direction, traces of LAGB-2 and LAGB-3 (lamella L2) are curvilinear and oriented at a relatively higher angle to X. Whilst the trace of LAGB-2 is oriented at a very high angle to X (angle θ varying between 87°- 61°), the trace of LAGB-3 is oblique to it (θ varying between 66°- 34°). Both LAGB's have striped patterns (Fig. 8c,d), which are finer compared to the pattern along LAGB-1 (Fig. 6a; lamella L1). These nano-stripes help in identifying a visible subgrain boundary zone that is apparently thinner than the LAGB-1.

HRTEM imaging of LAGB-2 with [112] zone axis followed by FT analysis show double reflection for $(\bar{1}3\bar{1})$, which yields a misorientation angle (α) of 0.9° (Supplementary data-3). This fits well with the ca 1° misorientation noted along the misorientation profile in parts of the ROI (Fig. 3c). The HRTEM image of LAGB-2 is replete with domains of varying contrast, some linear bands parallel to $[\bar{1}\bar{1}1]$, as well as blurred contrast (Supplementary data-3a). IFT and Bragg filtering of the image with $(\bar{1}3\bar{1})$ and $(1\bar{3}1)$ reflections reveal that these features are on account of dislocations (Supplementary data-3b to 3e). The dislocation density (ρ) is calculated to be 6.4×10^{-3} dislocations/nm^2. HRTEM imaging of the LAGB-3 with [112] zone axis also shows domains of blurred contrast and linear bands (Supplementary data-4a). The FT image and Bragg filtering of the HRTEM image with $(11\bar{1})$ and $(\bar{1}\bar{1}1)$ reflections shows that LAGB-3 has a denser network of defects (dislocations) (Supplementary data-4b to 4d) as compared to LAGB-2 (Supplementary data-3). The dislocation density for LAGB-3 is calculated to be 1.5×10^{-2} dislocations/nm^2.

6. Discussion

Our study has brought out interesting details related to orientation of trace of LAGB vis-à-vis X direction, dislocation density and nanostructures. The results can be exploited to better understand how nanostructures relate to shear strain at LAGB's, and thus open up further avenues of research such as numerical simulations of microstructures and forward modelling of microstructure development. These aspects are discussed in the present section. It may be noted that, although the data discussed here are for magnetite, similar implications can be expected for other minerals as well.

6.1. Shear strain along LAGB's in the kinematic reference frame

Our study shows the importance of LAGB orientations in the kinematic reference frame (XZ), and the nanostructures that develop in their vicinity in magnetite. The sense of shear in the studied BIF thin section is dextral and the elongation direction of the magnetite grain is parallel to the X direction (Fig. 2d). The trace of LAGB-1 (lamella L1) is straight (linear) and makes an angle (θ) of 4° with the X direction (Fig. 9a). Angular shear (ψ) along the LAGB can thus be calculated to be 86°, which yields a shear strain, γ (= tanψ) of 14.3. On the other hand, traces of LAGB-2 and LAGB-3 (lamella L2) are curvilinear. θ for trace of LAGB-2 and X-direction varies between 87° and 61°. Hence ψ along LAGB-2 varies between 3° and 29°, which yields γ of 0.05-0.55 (Fig. 9b). θ for the trace of LAGB-3 varies between 66°-34°; ψ is calculated to be 24°-56°, and hence γ is 0.44-1.48 (Fig. 9c). These calculations reveal that under the observed dextral shearing, the grain boundaries oriented at a lower angle to the X direction undergo greater shear strain than those at a high angle. Thus, empirically, $\theta_{LAGB\text{-}1} < \theta_{LAGB\text{-}3} < \theta_{LAGB\text{-}2}$, and hence, $\gamma_{LAGB\text{-}1} > \gamma_{LAGB\text{-}3} > \gamma_{LAGB\text{-}2}$. These considerations taken from the "*in-plane*" FIB lamella in magnetite are in agreement with the dextral shear sense determined from quartz CPO in the same XZ thin section (Fig. 2). This also implies that the magnetite and quartz were subjected to the same deformation.

6.2. Dislocation density vs. shear strain at magnetite LAGB

It was mentioned earlier (section 3) that the KAM map (Fig. 3b) is a well-known gauge of microscale deformation and the location from where FIB lamella L1 and L2 were excavated is shown in the inset of Fig. 9a. It is obvious from the KAM map that the LAGB's are represented by high KAM values. Additionally, it is also known that KAM and geometrically necessary dislocation (GND) density are interdependent thus implying that LAGB's in magnetite with high KAM value also have high GND density (e.g., Moussa et al., 2015; Kundu et al., 2020). However, it is from the TEM data and the dislocation density calculations presented above that we are able to observe and unequivocally establish that the orientation of LAGB, shear strain and dislocation density are inter-related.

The present study helps establish a positive relation between shear strain (γ) and dislocation density (ρ). There are large numbers of dislocations in the vicinity of LAGB-1 (lamella L1) and ρ is calculated to be in the order of 10^{-1} dislocations/nm^2 (Fig. 7; also see supplementary data-2). Further, as discussed above (section 7.1), the shear strain (γ) is 14.3 (Fig. 9a). Compared to the LAGB-1 (lamella L1), the LAGB-2,3 (lamella L2) have fewer dislocations and a lower ρ (Supplementary data-3,4). For LAGB-2, ρ is of the order of 10^{-3} dislocations/nm^2 (Supplementary data-3b) while γ_{LAGB-2} varies between 0.05-0.55 (Fig. 9b). ρ for LAGB-3 is of the order of 10^{-2} dislocations/nm^2 (Supplementary data-4b) while γ_{LAGB-3} varies between 0.44-1.48 (Fig. 9c). Our data shows that there is a difference of an order of magnitude in the dislocation density between the three LAGB's. Since, both the FIB lamella investigated here (L1 and L2) are ~50 nm thin, the variation in such orders of magnitude in dislocation densities of the different LAGB's cannot be attributed to thickness variations of thin film, and we infer that strain is the critical parameter for this. The empirical evidence presented in this study on magnetite clearly shows that there is a positive correlation between grain boundary trace orientation vis-à-vis X-direction of strain ellipsoid, shear strain and dislocation density. For $\gamma_{LAGB-1} > \gamma_{LAGB-3} > \gamma_{LAGB-2}$, the dislocation densities are $\rho_{LAGB-1} > \rho_{LAGB-3} > \rho_{LAGB-2}$. The shear strain rate ($\dot{\gamma}$) is related to the dislocation density, the Burger's vector (b), and the velocity of dislocation (v) by Orowan's equation ($\dot{\gamma} = b\rho v$) (e.g., Davoudi and Vlassak, 2018; also see Karato, 2008). Accordingly, ρ increases with $\dot{\gamma}$ (= γ/t), implying dislocation density is directly proportional to shear strain. Even in the case of recovery, where dislocation motion is considered to glide in a "jerky" fashion (spurt-like dislocation motion) following the Bailey-Orowan equation, there is a positive correlation between strain and dislocation density (Ojediran and Ajaja, 1988). Also, in metals that undergo dynamic recovery during hot and cold compression, the dislocation density has been reported to increase with strain (Yamaguchi and Yonemura, 2021). In light of the above cited previous works in materials science, our inference of the positive correlation between ρ and γ for the LAGBs in magnetite is justified (see section 7.3 for further discussion and validation of this from numerical simulations in halite).

Apart from the above, our TEM investigation also reveals that the LAGB's in magnetite are marked by stripes (identified as dislocations from FT and Bragg-filtering; see section 5), thus defining a subgrain boundary zone of various apparent thicknesses (Figs. 6a for LAGB-1; Figs. 8c,d for LAGB-2,3). Amongst the three LAGB's investigated here, LAGB-1 (Lamella L1) has the maximum γ and ρ and is characterized by a relatively thick striped subgrain boundary zone as compared to the other two LAGB's (Lamella L2), which have lower γ and ρ. Although the LAGB inclination in 3D can influence its 2D appearance on the thin film (FIB lamella), the dislocation density is independent of the inclination. Therefore, considering all the above empirical observations, we are inclined to raise a scientific question that can be debated in future "*are LAGB's analogous to zones of strain localization?*". The latter are manifested at all scales (Poirier, 1980) - in the field as mesoscopic scale shear zones (e.g., Ramsay and Huber, 1983) and under the microscope as microscale shear zones characterized by shear bands, oblique grain shape fabric etc. (e.g. Passchier and Trouw, 2005) or sometimes even as shear bands within crenulation cleavage zones (Mamtani et al., 1999). Fig. 9d is a schematic representation of an outcrop scale structure that structural geologists commonly encounter in the field. It shows a field foliation that curves into a zone of strain localization (shear zone). Thus, the shear strain (γ) increases towards the zone of strain localization, as the angle between the foliation and the shear zone decreases; this is similar to the empirical relation noted for angle between LAGB's and γ (Figs. 9a-c). It is interesting to note that (a) mesoscopic zones of shear/strain localization are known to be associated with strain hardening that causes them to thicken (e.g., Means, 1995; Vitale and Mazzoli, 2008) and (b) at the microscopic scale, strain hardening is a result of increased dislocation density (Nicolas and Poirier, 1976; Graça et al., 2008). Therefore, the greater apparent thickness of grain boundary zone at LAGB-1 and its higher dislocation density, as compared to the other two LAGB's maybe a manifestation of varied intensities of strain localization and related strain hardening. This needs further investigation.

6.3. Dislocation density vs. orientation of LAGB – support from numerical modelling

It has been shown that $\theta_{LAGB\text{-}1} < \theta_{LAGB\text{-}3} < \theta_{LAGB\text{-}2}$ and $\rho_{LAGB\text{-}1} > \rho_{LAGB\text{-}3} > \rho_{LAGB\text{-}2}$. In order to test this, we further postprocessed and analysed the numerical simulations of deformation of halite polycrystalline aggregates presented in Gomez-Rivas et al. (2017), in order to study the relationship between θ_{LAGB} and the predicted dislocation density. Halite was chosen because it (a) also belongs to the cubic crystal system like magnetite, (b) also undergoes slip on {110}, {100} and {111} planes (Gomez-Rivas et al., 2017) like magnetite (Charpentier et al., 1968; Hennig-Michaeli and Siemes, 1975, 1982, Banfield et al., 1994; Lindquist et al., 2015) and (c) is numerically very well investigated (e.g. Gomez-Rivas et al., 2017). Moreover, halite has been extensively studied as an analogue for the deformation and recrystallization of other minerals (e.g. Guillope & Poirier, 1979; Drury and Urai, 1990; Trimby et al., 2000; Linckens et al., 2018). The numerical simulations were carried out using the full-field crystal viscoplastic approach based on the fast Fourier transform that simulates dislocation glide (VPFFT; Lebensohn and Rollet, 2020), integrated into the software platform ELLE (Piazolo et al., 2019). Details of the modelling approach can be found in Gomez-Rivas et al. (2017). The initial microstructure with a random distribution of crystal orientations (Fig.10a) was subjected to dextral simple shear deformation until a shear strain of γ=1. In order to compare the influence of dynamic recrystallisation on the final microstructure, two simulations were developed: one including recovery and polygonization (called *recovery*) and another simulation affected only by dislocation glide (called *no_recovery*). Figure 10 shows the section of the grain boundary network and crystal orientation of the microstructures, where the horizontal is X. As shown in Fig. 10, the implementation of recovery and polygonization reduces intracrystalline heterogeneities, and thus misorientation, inside grains (see comparison of figures 10b and 10c). In order to investigate the relationship between θ_{LAGB} and the dislocation density predicted by the model, six grains were selected (grains A to F in Fig 10). We measured the angle θ_H between the LAGB's and X (the horizontal direction) of these halite grains and calculated the dislocation densities (ρ) across these LAGB's using ELLE-VPFFT software; the reader is referred to Llorens et al. (2016) for details. Plots of dislocation density fields for individual grains in the *no_recovery* and *recovery* simulations are shown in Supplementary data-5, respectively. These plot fields were done using the texture calculation toolbox MTEX (http://mtex.googlecode.com; Bachmann et al., 2010). Figure 10d,e shows that in our numerical experiments, LAGB's with low θ_H have high ρ, thus supporting the observations in the magnetite LAGB's observed under TEM.

6.4. Slip systems in magnetite and their relation to LAGB orientation

There are several past studies that have focused on evaluating the dominant slip systems in experimentally deformed magnetite (e.g., Charpentier et al., 1968, Hennig-Michaeli and Siemes, 1975, 1982; Muller and Siemes, 1972). A few experimental studies have also dealt with microstructures and magnetite slip systems (e.g., Banfield et al., 1994; Till and Moskowitz, 2014; Lindquist et al., 2015). These experimental studies have established that the dominant slip in magnetite occurs along {111} , {100} and {100} planes. In contrast, the present TEM investigation is done on a naturally (tectonically) deformed magnetite grain in the BIF sample. Our study reveals that the LAGB-1 (lamella L1) is oriented sub-parallel to $[31\bar{1}]$ direction (Figs. 6, 7). On the other hand, the LAGB-2,3 in lamella L2 are oblique to the crystallographic direction (Supplementary data-3,4). The orientation of principal stresses relative to crystallographic orientation in a grain is known to exert an important control over the activation of magnetite slip systems (Till and Moskowitz, 2014). Since the lamellae in the present study have been excavated parallel to the XZ reference frame of the strain ellipsoid, we have useful information about the orientation of each investigated grain boundary with respect to the crystal lattice directions as well as the X direction. Hence, we can also relate each segment of a particular grain boundary in an HRTEM image with the kinematic reference frame. In the case of LAGB-1 (lamella L1), it is not only at a low angle to X direction (section 7.1) but also is sub-parallel to a lattice plane, and as discussed above (section 7.2), has a higher dislocation density (in the order of 10^{-1} dislocations/nm^2). Conversely, the LAGB-2,3 are oriented at a higher angle to X (as compared to LAGB-1; section 7.1), are oblique to the lattice plane, and have a lower dislocation density (in the order of 10^{-2} to 10^{-3} dislocations/nm^2). Our empirical observations, therefore, indicate that the orientation of the grain boundaries with respect to the lattice planes may also be an important parameter that could control the dislocation density, an aspect that has been supported by numerical simulations as well (section 6.2). Finally, we would like to state that these results hold considerable promise for future scope of micro-/ nano- structural research, where TEM data from a tectonically deformed mineral could be integrated with experimental results to further analyze Burgers vector and slip systems, and relate these to the kinematic reference frame.

7. Conclusions

Most previous studies of grain boundaries and nano-structures under TEM have normally been conducted in thin films that were excavated perpendicular to the plane of view. However, structural geologists prefer to look at microstructures under the petrological as well as scanning electron microscope in rock thin sections that are prepared parallel to the kinematic reference frame (XZ of the strain ellipsoid). There are only very limited studies that have explored the possibility of excavating thin films parallel to the plane of view, particularly parallel to the kinematic reference frame of tectonically deformed rocks. This is important to better appreciate kinematics and relate structures from the hand-specimen (macroscopic scale) through microscopic scale (light microscope and SEM) to the nano-scale (TEM) keeping full track of the extension direction (X) in the kinematic reference frame. We have filled this lacuna through the present paper by excavating in-plane site specific FIB lamella from kinematic reference frame of magnetite hosted in BIF thin section. The elaborate modus operandi presented allows replication of the methodology by any interested structural geologist keen to work on nanostructures, which is an aspect that was missing in previous studies.

The procedure involved the following steps – (1) preparation of a BIF rock thin section parallel to the kinematic reference frame (XZ); in our study the latter was identified from AMS studies, but in rocks containing stretching lineations and foliations, it can be recognized based on field data (2) SEM-EBSD analysis of magnetite and quartz grains in the thin section (3) recognition of strained areas and LAGB's within magnetite and the identification of ROI for site-specific TEM studies (4) "*in-plane*" FIB lamella excavation from the region of interest from the plane of view of the rock thin section (5) TEM investigation of nanostructures at LAGB's in the "*in-plane*" FIB lamellae. The *modus operandi*, though time-consuming and elaborate, provides the best possibility to investigate nanostructures in minerals in the kinematic reference frame. The critical aspect is that we kept track of the X direction in the plane of view (XZ) at each stage of analysis. Hence, the present TEM investigation brings to light several empirical relations between trace of the grain boundary, its angle (θ) with X (elongation) direction of strain ellipsoid, shear strain (γ) and dislocation density (ρ) for the three investigated magnetite low angle grain boundaries (LAGB-1, LAGB-2 and LAGB-3). Following are the important conclusions from the study.

a. Data for LAGB-1, LAGB-2 and LAGB-3 in the magnetite indicates $\theta_{LAGB-1} < \theta_{LAGB-3} < \theta_{LAGB-2}$, $\gamma_{LAGB-1} > \gamma_{LAGB-3} > \gamma_{LAGB-2}$ and $\rho_{LAGB-1} > \rho_{LAGB-3} > \rho_{LAGB-2}$. These empirical relations imply increase in shear stain and dislocation density in the vicinity of magnetite LAGB with reduction in the angle between LAGB and the extension direction of strain.
b. The empirical observations from magnetite in the BIF sample are supported and validated by full-field numerical simulations of polycrystalline halite, where the dislocation density is observed to increase with the decrease in θ_H (angle between halite LAGB and shear plane).
c. The spatial geometry of grain boundaries vis-à-vis principal strain axes and lattice planes in natural tectonically deformed rocks can be an important factor that can control dislocation density build-up.
d. Structural Geologists commonly collect oriented field samples and prepare oriented thin sections, where the kinematic reference frame can also be related to the geographical reference frame. The *modus operandi* presented in this study provides a possibility to excavate "*oriented site-specific in-plane*" FIB lamellae from a mineral so that nanostructures under TEM can be investigated not only in the kinematic reference frame, but also related to the geographical reference frame.

Compared to level of TEM studies that are common in materials science, the studies on earth materials are rather limited, often due to their fine-scale heterogeneity (Lee, 2010). Despite FIB method being in vogue for several decades now, not many geoscientists have explored looking at structures in rock thin films, and hardly anyone to date has tried to relate nanostructures with LAGB geometry and dislocation density in a thin film prepared parallel to the kinematic reference frame. This study is the first attempt, and as briefly summarized by Mamtani et al. (2022) and Mamtani (2023; in-press), we believe that it holds considerable promise to further look at different nanostructures and characterize them under different imaging conditions, just like is commonly done by materials scientists. We envisage that similar to materials sciences, the knowledge of nanostructures at grain boundaries in minerals could be useful to better understand their control on physical properties and rheology of the host rock. Some grain boundaries in metals are even known to be locales of formation of fatigue cracks (e.g., Sangid et al., 2011; Li et al., 2016). Thus, in geosciences, TEM studies of site-specific "*in-plane*" FIB lamella excavated from across different types of grain boundaries can enhance our understanding of nanoscale processes. This is also expected to assist in forward modelling of ductile-to-brittle deformation from the nanoscale to the macroscale.

Acknowledgments:

This study is an outcome of a collaborative research project funded by the Alexander von Humboldt Foundation (Germany) under its Research Group Linkage Program awarded to MAM, AK and CH. Amarnath Dandapat (Department of Geology and Geophysics, IIT Kharagpur, India) is thanked for preparing well-polished samples for EBSD analysis. Thanks are due to Niloy Bhowmik for helping with SEM-EBSD analysis at the Central Research Facility (IIT Kharagpur, India). We are grateful to Heike Störmer for helping with TEM analysis at the Laboratory for Electron Microscopy, Karlsruhe Institute of Technology

(Karlsruhe, Germany). EGR acknowledges the Ramón y Cajal fellowship (RYC2018-026335-I), funded by the Spanish Ministry of Science and Innovation (MCIN)/State Research Agency of Spain (AEI)/European Social Fund (10.13039/501100011033), and the research project PID2020-118999GB-I00, also funded by the MCIN/AEI/10.13039/501100011033. Reviews by anonymous reviewers and editorial handling by Eugenio Fazio are gratefully acknowledged.

Appendix-1: SEM-EBSD measurements – acquisition and data processing

In the present study, SEM-EBSD analysis of quartz and magnetite was performed in the BIF rock thin section that was polished for 6 hours with non-crystallizing colloidal silica solution. Subsequently, the thin section was coated with 5 nm carbon before loading it into the SEM chamber. EBSD patterns were acquired at 30 kV accelerating voltage, 1.49 x 10^{-6} mbar system vacuum, and ~17 mm working distance using Carl Zeiss Auriga Compact FEG-SEM fitted with NordlysMax2 EBSD detector (Oxford instruments, UK) housed in the Central Research Facility (CRF, IIT Kharagpur, India). Quartz and magnetite crystallography data were acquired automatically using AZtecHKL (Oxford instruments, UK). Acquired data were processed using the software AZtecCrystal (Oxford Instruments, UK). Post processing involved a low level noise reduction, preparation of Inverse Pole Figure (IPF) and Kernel Average Misorientation (KAM) maps and pole figures (lower hemisphere equal area projections) of quartz *c*-axis $\{0001\}$, quartz *a*-axes $\{11\bar{2}0\}$, as well as magnetite crystal axes viz. $\{100\}$, $\{110\}$ and $\{111\}$. Whilst the quartz CPO were used to verify the kinematic reference frame (XZ of the strain ellipsoid; see section 2), the magnetite IPF and KAM maps were used to identify the large magnetite grain for TEM investigation (following lamella excavation using FIB; see section 3). Several misorientation profiles were prepared from the selected magnetite grain and eventually the profile UV (Fig. 3a-c) was selected because of several subgrain boundaries along it. This helped identify the exact region of interest from which "*in-plane*" site-specific FIB lamella L1 and L2 were excavated for TEM investigation.

References

Agar, S., Lloyd, G., 1997. Deformation of Fe-Ti oxides in gabbroic shear zones from the Mark area, in Proc. ODP, Sci. Results 153, 123-141.

Archanjo C. J., Launeau P., Bouchez J. L., 1995. Bulk magnetic fabric versus shape fabrics of magnetite and biotite in magnetite-bearing pluton (Gameleiras, Northeast Brazil). Phys. Earth and Planet. Inter. 89, 63-75.

Atkinson, B.K., 1977. The kinetics of ore deformation: its illustration and analysis by means of deformation-mechanism maps. Geologiska Föreningens Förhandlingar 99, 186–197.

Bachmann, F., Hielscher, R., Schaeben, H. 2010. Texture analysis with MTEX—Free and open source software toolbox. Solid State Phenomena, 160, 63–68. https://doi.org/10.4028/www.scientific.net/SSP.160.63

Banfield J. F., Wasilcwski P.J., and Vebken D. R. (1994) TEM study of relationships between the microstructures and magnetic properties of strongly magnetised magnetite and maghemite. Amer. Mineral. 79, 654-667.

Bella Nké, B.E., Njanko, T., Mamtani, M.A., Njonfang, E., Rochette, P., (2018). Kinematic evolution of the Mbakop Pan-African granitoids (Western Cameroon-Domain): an integrated AMS and EBSD approach. Journal of Structural Geology, 111, 42-63.

Bjørlykke, A., Olerud, S., Sandstad, J.S., 1985. Metallogeny of Finnmark, North Norway. Norges Geologiske Undersøkelse, Bulletin 403, 183-196.

Blenkinsop, T.G. 2000. Deformation microstructures and mechanisms in minerals and rocks. Kluwer Academic Publishers, Dordrecht.

Borradaile, G.J., 2001. Magnetic fabrics and petrofabrics; their orientation distributions and anisotropies. Journal of Structural Geology, 23. 1581-1596.

Borradaile, G.J., Jackson, M.J. Structural geology, petrofabrics and magnetic fabrics (AMS, AARM, AIRM). Journal of Structural Geology 32, 1519-1551.

Bouchez, J-L., 1978. Preferred orientations of quartz <a> axes in some tectonites: kinematic inferences. Tectonophysics, 49, T25-T30.

Bouchez, J-L., Nicolas, A., 2021. Principles of rock deformation and tectonics. Oxford University Press, UK.

Bons, P.D., Koehn, D., Jessell, M.W., 2008. Microdynamics Modelling. Lecture Notes in Earth Sciences 106, Springer, Berlin.

Bouchez, J.L., Duval, P., 1982. The fabric of polycrystalline ice deformed in simple shear: experiments in torsion, natural deformation and geometrical interpretation. Texture, Stress, and Microstructure 5, 171-90.

Boyd, R., Bjerkgård, T., Nordahl, B., Schiellerup, H., 2016. Mineral resources in the Arctic. NGU-Geological Survey of Norway.

Brewer, L.N., Field, D.P., Merriman, C.C., 2009. Mapping and assessing plastic deformation using EBSD. In: Schwartz, A.J., Kumar, M., Adams, B.L., Field, D.P. (eds.). Electron Backscatter Diffraction in Materials Science; 251–262.

Bugge, J.A.W., 1980. The Sydvaranger type of quartz banded iron ore, with a synopsis of Precambrian geology and ore deposits of Finnmark. Geological Survey of Finland, Bull, 307, 15-24.

Charpentier, Ph., Rabbe, P., Manenc, J., 1068. Mise en evidence de la plasticite de la magnetite mesure de la durete en fonction de la temperature. Materials Research Bulletin, 3, 69-78.

Davoudi, K.M., Vlassak, J.J., 2018. Dislocation evolution during plastic deformation: Equations vs. discrete dislocation dynamics study. Journal of Applied Physics 123, 085302; https://doi.org/10.1063/1.5013213.

de Almeida Ribeiro, I., de Koning, M., 2021. Grain-boundary sliding in ice I_h: tribology and rheology at the nanoscale. The Journal of Physical Chemistry C, 125, 627–634; https://doi.org/10.1021/acs.jpcc.0c10032.

Drury, M.R., Urai, J.L. 1990. Deformation-related recrystallization processes. Tectonophysics, 172, 235-253.

Drury, M.R., Avé Lallemant, H.G., Pennock, G.M., Palasse, L.N., 2011. Crystal preferred orientation in peridotite ultramylonites deformed by grain size sensitive creep, Étang de Lers, Pyrenees, France. Journal of Structural Geology 33, 1776-1789; https://doi.org/10.1016/j.jsg.2011.10.002.

Ferré, E., Teyssier, C., Jackson, M., Thill, J.W., Rainey, E.S.G., 2003. Magnetic susceptibility anisotropy: A new petrofabric tool in migmatites. J. Geophys. Res., 108(B2), 2086, doi:10.1029/2002JB001790.

Ferré, E.C., Gébelin, A., Till, J.L., Sassier, C., Burmeister, K.C.y, 2014. Deformation and magnetic fabrics in ductile shear zones: A review. Tectonophysics 629, 179-188.

Ferreira, F., Hansen, L. N., Marquardt, K., 2021. The effect of grain boundaries on plastic deformation of olivine. Journal of Geophysical Research: Solid Earth, 126, e2020JB020273. https://doi.org/10.1029/2020JB020273.

Fliervoet, T.F., White, S.H., Drury, M.R., 1997. Evidence for dominant grain-boundary sliding deformation in greenschist- and amphibolite-grade polymineralic ultramylonites from the Redbank Deformed Zone, Central Australia. Journal of Structural Geology 19, 1495-1520.

Graça, S., Colaço, R., Carvalho, P.A., Vilar, R., 2008. Determination of dislocation density from hardness measurements in metals. Materials Letters 62, 3812–3814.

Giannuzzi, L.A., Stevie, F.A., 1999. A review of focused ion beam milling techniques for TEM specimen preparation. Micron 30, 197-204.

Giannuzzi, L.A., Stevie, F.A., 2005. Introduction to focused ion beams: instrumentation, theory, techniques, and practice. Springer, New York; doi: 10.1007/ b101190.

Gomez-Rivas, E., Griera, A., Llorens, M.-G., Bons, P.D., Lebensohn, R.A., Piazolo, S., 2017. Subgrain rotation recrystallization during shearing: insights from full-field numerical simulations of halite polycrystals. Journal of Geophysical Research: Solid Earth 122, 8810-8827. https://doi.org/10.1002/2017JB014508.

Goodwin, L.B., Wenk, H.-R., 1990. Intracrystalline folding and cataclasis in biotite of the Santa Rosa mylonite zone: HVEM and TEM observations. Tectonophysics, 172, 201-214.

Goswami, S., Mamtani, M.A., Rana, V., 2018. Quartz CPO and kinematic analysis in deformed rocks devoid of visible stretching lineations: an integrated AMS and EBSD investigation. Journal of Structural Geology 115, 270-283.

Heaney, P.J., Vicenzi, E.P., Giannuzzi, L.A., Livi, K.J.T., 2001. Focused ion beam milling: a method of site-specific sample extraction for microanalysis of Earth and planetary materials. Am. Mineral. 86, 1094–1099.

Hennig-Michaeli, C., Siemes, H., 1975. Zwillingsgleitung beim Magnetit. Neues Jahrbuch Mineralogie Abh. 123, 330–334.

Hennig-Michaeli, C., Siemes, H., 1982. Compression experiments on natural magnetite crystals at 200 °C and 400 °C at 400 MPa confining pressure. In: Issues in Rock Mechanics Proceedings, Twenty-Third Symposium on Rock Mechanics, the University of California, Berkeley, California, August 25-27, 1982, p. 380, Society of Mining Engineers of AIME, New York, NY.

Hillier, J., 1954. New Interference Phenomena in the Electron Microscopic Images of Plate-like Crystals, 527. National Bureau of Standards, pp. 413–416.

Hirth, G., Tullis, J., 1992. Dislocation creep regimes in quartz aggregates. Journal of Structural Geology 14, 145-159.

Hobbs, B.E., Means, W.D. and Williams, P.F., 1976. An Outline of Structural Geology. John Wiley & Sons, Inc.

Housen, B.A., van der Pluijm, B.A., Essene, E.J., 1995. Plastic behaviour of magnetite and high strains obtained from magnetic fabrics in the Parry Sound shear zone, Ontario Grenville Province. Journal of Structural Geology 17, 265–278.

Igami, Y., & Michibayashi, K. (2021). Transmission Kikuchi diffraction study of submicrotexture within ultramylonitic peridotite. Physics and Chemistry of Minerals, 48(10), 1-12. https://doi.org/10.1007/s00269-021-01161-7.

Johannesson, T., Thölén, A., 1970. On the influence of grain boundaries on mechanical properties, Philosophical Magazine, 21:174, 1223-1228, DOI: 10.1080/14786437008238506.

Johnson, C.L., Hÿtch, M.J., Buseck, P.R., Watson, B., 2004. Nanoscale Waviness of Low-Angle Grain Boundaries. Proceedings of the National Academy of Sciences of the United States of America, 101 (52), 17936-17939, https://www.jstor.org/stable/3374172.

Kamaya, M., 2011. Assessment of local deformation using EBSD: Quantification of accuracy of measurement and definition of local gradient. Ultramicroscopy 111, 1189-1199.

Karato, S., 2009. Deformation of earth materials: an introduction to the rheology of solid earth. Cambridge University Press.

Kogure, T., Raimbourg, H., Kumamoto, A., Fujii, E., Ikuhara, Y., 2014. Subgrain boundary analyses in deformed orthopyroxene by TEM/STEM with EBSD-FIB sample preparation technique. Earth, Planets and Space, 66:84, doi:10.1186/1880-5981-66-84.

Kontny, A., Engelmann, R., Grimmer, J.C., Greiling, R.O., Hirt, A., 2012. Magnetic fabric development in a highly anisotropic magnetite-bearing ductile shear zone (Seve Nappe Complex, Scandinavian Caledonides). International Journal of Earth Sciences 101, 671-692.

Kruhl, J. H., Wirth, R., Morales, L. F. G., 2013. Quartz grain boundaries as fluid pathways in metamorphic rocks, Journal of Geophysical Research: Solid Earth 118, 1957–1967, doi:10.1002/jgrb.50099.

Kundu, A., Field, D.P., Chakraborty, P.C., 2020. Effect of strain and strain rate on the development of deformation heterogeneity during tensile deformation of a solution annealed 304 LN austenitic stainless steel: An EBSD study. Materials Science and Engineering A 773, 138854, https://doi.org/10.1016/j.msea.2019.138854.

Langford, R.M., Petford-Long, A.K., 2001. Preparation of transmission electron microscopy cross-section specimens using focused ion beam milling. Journal of Vacuum Science & Technology A 19, 2186; https://doi.org/10.1116/1.1378072.

Law, R.D., 1986. Relationships between strain and quartz crystallographic fabrics in the Roche Maurice quartzites of Plougastel, western Brittany. Journal of Structural Geology 8, 493-515.

Lebensohn RA, Rollett AD. Spectral methods for full-field micromechanical modelling of polycrystalline materials. Computational Materials Science. 2020 Feb 15;173:109336.

Le Floch, A. 1969. Moiré pattern for a crystal containing a dislocation, Philosophical Magazine, 19:158, 429-430, https://doi.org/10.1080/14786436908217800.

Lee, M.R. 2010. Transmission electron microscopy (TEM) of Earth and planetary materials: A review. Mineralogical Magazine 74, 1-27. https://doi.org/10.1180/minmag.2010.074.1.1.

Li, C., Habler, G., Baldwin, L.C., Abart, R., 2018. An improved FIB sample preparation technique for site-specific plan-view specimens: A new cutting geometry. Ultramicroscopy 184, 310-317.

Li, L.L., Zhang, Z.J., Zhang, P., Yang, J.B., Zhang, Z.F., 2016. Distinct fatigue cracking modes of grain boundaries with coplanar slip systems. Acta Materialia 120, 120-129.

Linckens, J., Zulauf, G., Mertineit, M. 2018. The influence of a grain-shape fabric on the mechanical behaviour of rock salt: Results from deformation experiments. Tectonophysics 751, 73-82; https://doi.org/10.1016/j.tecto.2018.12.009.

Lindquist, A., Feinberg, J., Harrison, R., Loudon, J., Newell, A., 2015. Domain wall pinning and dislocations: investigating magnetite deformed under conditions analogous to nature using transmission electron microscopy. J. Geophys. Res. (Solid Earth) 120, 1415-1430.

Lister, G.S., Hobbs, B.E., 1980. The simulation of fabric development during plastic deformation and its application to quartzite: the influence of deformation history. Journal of Structural Geology 2, 355-371.

Liu, B., Eisenlohr, P., Roters, F., Raabe, D., 2012. Simulation of dislocation penetration through a general low-angle grain boundary. Acta Materialia 60, 5380–5390.

Llorens, M.G., Griera, A., Bons, P.D., Roessiger, J., Lebensohn, R., Evans, L. and Weikusat, I., 2016. Dynamic recrystallisation of ice aggregates during co-axial viscoplastic deformation: a numerical approach. Journal of Glaciology, 62, 359-377.

Llorens, M-G., Griera, A., Steinbach, F., Bons, P.D., Gomez-Rivas, E., Jansen, D., Roessiger, J., Lebensohn, R.A., Weikusat, I., 2017. Dynamic recrystallization during deformation of polycrystalline ice: insights from numerical simulations. Phil. Trans. R. Soc. A 375: 20150346. http://dx.doi.org/10.1098/rsta.2015.0346.

Lyu, M., Cao, S., Neubauer, F., Li, J., Cheng, X., 2020. Deformation fabrics and strain localization mechanisms in graphitic carbon-bearing rocks from the Ailaoshan-Red River strike-slip fault zone. Journal of Structural Geology 140, 104150.

Mainprice, D., Nicolas, A., 1989. Development of shape and lattice preferred orientations: application to the seismic anisotropy of the lower crust. Journal of Structural Geology 11, 175-189.

Mamtani, M.A., 2014. Magnetic fabric as a vorticity gauge in syntectonically deformed granitic rocks. Tectonophysics, 629,189-196.

Mamtani, M.A. (2023; in-press). SEM-EBSD studies of tectonically deformed rocks and kinematic analysis. In: Suwas, S. and Field, D.P. (Eds) *Advances in Microtexture: Measurements, Analyses, and Application*. Springer (in-press).

Mamtani, M.A., Greiling, R.O., Karanth, R.V., 1999. Are crenulation cleavage zones mylonites on the microscale? Journal of Structural Geology 21, 711-718.

Mamtani, M.A., Reznik, B., Kontny, A., 2020. Intracrystalline deformation and nanotectonic processes in magnetite from a naturally deformed rock. Journal of Structural Geology, 135, 104045 (https://doi.org/10.1016/j.jsg.2020.104045). Mamtani, M.A., Piazolo, S., Kontny, A., Greiling, R.O. and Hrouda, F., 2011. Process of magnetite fabric development during granite deformation. Earth and Planetary Science Letters 308, 77-89.

Mamtani, M.A., Pal, T. and Greiling, R.O., 2013. Kinematic analysis using AMS data from a deformed granitoid. Journal of Structural Geology 50, 119-132.

Mamtani, M.A., Piazolo, S., Kontny, A., Greiling, R.O. and Hrouda, F., 2011. Process of magnetite fabric development during granite deformation. Earth and Planetary Science Letters, 308, 77-89.

Mamtani, M.A., Abhijith, V., Lahiri, S., Rana, V., Bhatt, S., Goswami, S. and Renjith, A.R., 2017. Determining the reference frame for kinematic analysis in S-tectonites using AMS. Journal of the Geological Society of India 90, 5-8.

Mamtani, M.A., Bhatt, S., Rana, V., Sen, K., Mondal, T.K., 2019. Application of AMS in understanding regional deformation fabric development and granite emplacement: examples from Indian cratons. In: Dey, S. and Moyen, J-F (eds.) Archean Granitoids of India: Windows into Early Earth Tectonics. Geological Society of London Special Publications 489, 275-292 (https://doi.org/10.1144/SP489-2019-292).

Mamtani, M.A., Kontny, A., Hilgers, C., Reznik, B., Wenzel, O., Müller, E., Störmer, H., Renjith, A.R., 2022. Nanostructures in oriented thin films – from microtectonics to nanotectonics and nanokinematics in deformed rocks. Abstract Book, 23rd International Conference on Deformation Mechanisms, Rheology and Tectonics (DRT), Catania (Italy), Società Geologica Italiana, Roma, p. 18. https://doi.org/10.3301/ABSGI.2022.01%20.

Mayer, J., Giannuzzi, L.A., Kamino, T. Michael, J., 2007. TEM Sample Preparation and FIB-Induced Damage. MRS Bulletin 32, 400–407. https://doi.org/10.1557/mrs2007.63.

McLaren, A.C., 1991. Transmission Electron Microscopy of Minerals and Rocks. Cambridge University Press, New York.

Means, W.D., 1995. Shear zones and rock history. Tectonophysics 247, 157–160.

Mitsuishi, T., Nagasaki, H., Uyeda, R., 1951. A new type of interference fringes observed in electron-micrographs of crystalline substance. Proc. Jpn. Acad. 27, 86–87.

Moussa, C., Bernacki, M., Besnard, R., Bozzolo, N., 2015. About quantitative EBSD analysis of deformation and recovery substructures in pure Tantalum. IOP Conf. Series: Materials Science and Engineering 89 (2015) 012038 doi:10.1088/1757-899X/89/1/012038.

Natland, J., 2002. Magnetic susceptibility as an index of the lithology and composition of gabbro, ODP Leg 176, Hole 735B, Southwest Indian Ridge, Proc. ODP, Sci. Results 176, 1-69.

Nicolas, A., Poirier, J.P. 1976. Crystalline plasticity and solid state flow in metamorphic rocks. Wiley, New York.

Ohring, M., 1995. Engineering Materials Science. Elsevier. https://doi.org/10.1016/B978-0-12-524995-9.X5023-5.

Ojediran, S.O., Ajaja, O., 1988. The Bailey-Orowan equation. Journal of Materials Science 23, 4037-4040.

Passchier, C.W., Myers, J.S., Kröner, A., 1990. Field geology of high-grade gneiss terrains. Springer-Verlag, Berlin.

Passchier, C.W., Trouw, R.A.J., 2005. Microtectonics. Springer, Berlin.

Pennock, G., Drury, M., 2020. Shear coupled grain boundary migration as a deformation mechanism in minerals., EGU2020-7681, https://doi.org/10.5194/egusphere-egu2020-7681.

Piazolo, S., Jessell, M.W., Bons, P.D., Evans, L., Becker, J.K., 2010. Numerical Simulations of Microstructures Using the Elle Platform: A Modern Research and Teaching Tool.

Piazolo, S., Bons, P.D., Griera, A., Llorens, M.G., Gomez-Rivas, E., Koehn, D., Wheeler, J., Gardner, R., Godinho, J.R., Evans, L. and Lebensohn, R.A., 2019. A review of numerical modelling of the dynamics of microstructural development in rocks and ice: Past, present and future. Journal of Structural Geology, 125, pp.111-123.

Poirier, J.P., 1980. Shear localization and shear instability in materials in the ductile field. Journal of Structural Geology 2, 135-142.

Prior, D.J., Bestmann, M., Halfpenny, A., Mariani, E., Piazolo, S., Tullis, J., Wheeler, J., 2004. Recrystallization and grain growth in rocks and minerals. Materials Science Forum 467-470, 545-550.

Ramsay, J.G., Huber, M.I., 1983. The techniques of modern structural geology, volume-1: Strain analysis. Academic Press, London.

Renjith, A.R., Mamtani, M.A. and Urai, J.L., 2016. Fabric analysis of quartzites with negative magnetic susceptibility - does AMS provide information of SPO or CPO of quartz? Journal of Structural Geology 82, 48-59.

Reznik B., Kontny A., Fritz J., Gerhards U., 2016. Shock- induced deformation phenomena in magnetite and their consequences on magnetic properties. Geochemistry Geophysics Geosystems, 17, 1–20.

Sangid, M.D., Maier, H.J., Sehitoglu, H., 2011. The role of grain boundaries on fatigue crack initiation – An energy approach. International Journal of Plasticity 27, 801–821.

Schmid, S.M., Casey, M., 1986. Complete fabric analysis of some commonly observed quartz [c]-axis patterns. In: Hobbs, B.E., Heard, H.C. (Eds.), Mineral and Rock Deformation: Laboratory Studies. Geophysical Monograph, vol. 36, 263-286.

Schnieder, C.A., Rasband, W. S., Eliceiri, K. W., 2012. NIH Image to ImageJ: 25 years of image analysis. Nature Methods 9, 671–675. http://www.nature.com/articles/nmeth.2089.

Shigematsu, N., Prior, D.J., Wheeler, J., 2006. First combined electron backscatter diffraction and transmission electron microscopy study of grain boundary structure of deformed quartzite. Journal of Microscopy, 224, 306-321; https://doi.org/10.1111/j.1365-2818.2006.01697.x.

Sen, K., Mamtani, M.A., 2006. Magnetic fabric, shape preferred orientation and regional strain in granitic rocks. Journal of Structural Geology 28, 1870-1882.

Stadelmann, P. A., 1987. EMS - a software package for electron diffraction analysis and HREM image simulation in materials science. Ultramicroscopy 21, 131–145, https://www.sciencedirect.com/science/article/pii/0304399187900805.

Stipp, M., Stünitz, H., Heilbronner, R., Schmid, S.M., 2002. The eastern Tonale fault zone: a "natural laboratory" for crystal plastic deformation of quartz over a temperature range from 250 to 700 °C. Journal of Structural Geology 24, 1861-1884.

Takeshita, T., Hara, I., 1998. *c*-Axis fabrics and microstructures in a recrystallized quartz vein deformed under fluid-rich greenschist conditions. Journal of Structural Geology 20, 417-431.

Tarling, D.H., Hrouda, F., 1993. The Magnetic Anisotropy of Rocks. Chapman and Hall, London.

Till, J.L., Moskowitz, B., 2013. Magnetite deformation mechanism maps for better prediction of strain partitioning. Geophysical Research Letters, 40, 697-702.

Till, J.L., Moskowitz, B.M., 2014. Deformation microstructures and magnetite texture development in synthetic shear zones. Tectonophysics 629, 211-223.

Till, J.L., Moskowitz, B.M., Jackson, M.J., 2012. High-temperature magnetic fabric development from plastically deformed magnetite in experimental shear zones. Geophysical Journal International 189, 229–239.

Trepmann, C., Seybold, L., 2019. Deformation at low and high stress-loading rates. Geoscience Frontiers 10, 43-54.

Trimby, P. W., Drury, M. R., Spiers, C. J. 2000. Recognising the crystallographic signature of recrystallization processes in deformed rocks: A study of experimentally deformed rocksalt. Journal of Structural Geology 22, 1609–1620. https://doi.org/10.1016/S0191-8141(00)00059-6.

Tullis, J. 1977. Preferred orientation of quartz produced by slip during plane strain. Tectonophysics 39, 87-102.

Urai, J., Means, W.D., Lister, G.S., 1986. Dynamic recrystallization of minerals. In: Heard HC, Hobbs BE (eds.) Mineral and rock deformation: laboratory studies. Geophysical Monograph, vol. 36. The Paterson Volume: American Geophysical Union, 161-200.

Vitale, S., Mazzoli, S., 2008. Heterogeneous shear zone evolution: The role of shear strain hardening/softening. Journal of Structural Geology 30, 1383-1395.

Viti, C., Brogi, A., Liotta, D., Mungnaioli, E., Spiess, R., Dini, A., Zucchi, M., Vannuccini, G., 2016. Seismic slip recorded in tourmaline fault mirrors from Elba Island (Italy). Journal of Structural Geology 86, 1-12.

Wang, Y., Ho, J.C., Liao, X.Z., Li, H.Q., Ringer, S.P., Zhu, Y.T., 2009. Mechanism of grain growth during severe plastic deformation of a nanocrystalline Ni–Fe alloy. Applied Physics Letters 94:011908-011908-3, https://doi.org/10.1063/1.3065025.

Wheeler, J., Mariani, E., Piazolo, S., Prior, D.J., Trimby, P., Drury, M.R., 2009. The weighted Burgers vector: a new quantity for constraining dislocation densities and types using electron backscatter diffraction on 2D sections through crystalline materials. Journal of Microscopy 233, 482–494.

Williams, D.B., Carter, C.B. (2009). Transmission Electron Microscopy - A textbook for Materials Science. 2nd Edition, Springer.

Xypolias, P., 2010. Vorticity analysis in shear zones: A review of methods and applications. Journal of Structural Geology 32, 2072-2092.

Yamaguchi, I., Yonemura, M., 2021. Metallurgical and Materials Transactions A, 52A, 3517, https://doi.org/10.1007/s11661-021-06323-4.

Williams, D.B., Carter, C.B., 2009. Transmission Electron Microscopy - A Textbook for Materials Science, second ed. Springer.

Figure Captions

Figure-1: (a) Hand specimen of the BIF sample (Norway) investigated in this study. The vertical banding defines the foliation in the specimen. AMS analysis of a cube (b) prepared from the hand specimen was carried out to identify the three principal axes of the AMS ellipsoid ($K_1>K_2>K_3$). The latter are plotted in the lower hemisphere equal area projection in (c) and for easy visualization are also superimposed on the cube in (b). The AMS data indicates that in the specimen reference frame, the magnetic foliation (K_1K_2 plane) is vertical (parallel to the banding shown by dashed line in Fig. 1b) and the magnetic lineation (K_1) is horizontal. (d) Photomicrograph (partially crossed polarizers) documenting the banded character of the BIF sample in a rock thin section prepared parallel to the K_1K_3 plane of the AMS ellipsoid. The dark minerals are magnetite and these layers alternate with quartz bands (lighter in colour). The bottom of the rock thin section below the marker line OP was chosen for further investigation.

Figure-2: (a) Forescatter detector (FSD) image of the broad area of BIF thin section showing bands of magnetite rich layers (light) and quartz (darker). The image is from the bottom part the thin section (below marker line OP in Fig. 1d). Arrow points to a magnetite grain that has been the focus of the present investigation. (b) Inverse pole figure (IPF) map of quartz from the entire thin section area of (a); boxed area marks the magnetite grain that was shown by arrow in (a). Note that the thin section is parallel to K_1K_3 reference plane of AMS ellipsoid, which is shown in (a) and (b) and the banding (foliation) trace defines the K_1K_2 (magnetic foliation) trace. (c) Lower hemisphere equal area projection of quartz CPO (*c*- and *a*- axes) in

K_1K_3 reference frame. The vertical line is the magnetic foliation trace (K_1K_2). The quartz CPO indicates dextral shearing with basal<a> and rhomb<a> being the dominant slip systems. This establishes the parallelism between the AMS ellipsoid (K_1>K_2>K_3) and strain ellipsoid (X>Y>Z), thus indicating K_1K_3 section is parallel to the kinematic reference frame, henceforth referred as XZ section in (e) and (f) as well as subsequent figures. (d). IPF map of magnetite in the same thin section area as in (b). EBSD data acquisition for this entire frame was done at 5 μm step size. (e) Lower hemisphere equal area projection of magnetite crystallographic axes viz. {100} and {110}. (f) Forescatter detector (FSD) image of the magnetite showing presence of some orientation contrast parts of the grain (shown by white arrows).

Figure-3: (a) and (b) are, respectively, the inverse pole figure (IPF) and kernel average misorientation (KAM) map of the magnetite investigated in detail in this study. UV marks the line along which crystallographic misorientation profile was prepared from IPF map data, which is shown in (c). The same profile line (UV) is also shown in the KAM map (b), for reference. ROI and ROM in (c) represent region of interest and region of microcracks, respectively. The ROI comprises low angle grain boundaries (LAGB's); locations of FIB lamella L1 and L2 are shown. See text for detail description. (d) SE image of the magnetite documenting the ROM and the absence of detectable microcracks in the ROI.

Figure-4: (a) Documentation of initial step of *in situ* lift out (INLO) FIB lamella extraction from ROI within magnetite in the BIF rock thin section. (a-i) 3D schematic representation of the plan view of BIF thin section and the magnetite grain in the kinematic reference frame. The plan view is XZ section while the banding is the trace of XY plane (X>Y>Z are the three principal axes of the strain ellipsoid equivalent to K_1>K_2>K_3 principal axes of the AMS ellipsoid). (a-ii) Plan-view (XZ reference frame) visualization of the IPF map from EBSD data of the magnetite grain selected for detailed investigation. The ROI lies within the dashed box. The first step of INLO FIB lamella extraction is to deposit platinum straps on the area to be excavated. The platinum straps marked L1 and L2 mark FIB lamella 1 and 2, respectively in (a-iii). As shown in the inset in a-iii, these two lamella are from the ROI (dashed box) containing the LAGB's. Two additional areas were also covered by platinum straps (bk1 and bk2) the reason for which is explained in the text (section-4). (b) SEM images documenting the INLO FIB lamella extraction parallel to the plane of view (XZ section) of L1 (b-i) and L2 (b-ii). In both the images the arrow "*M*" on the bottom left marks the point of attachment/glueing (with platinum) between the tungsten needle (marked TN) and the excavated FIB lamella. After each INLO, each lamella was mounted on respective copper grids for further thinning. The view of the ROI in the thin section after "*in-plane*" FIB lamella excavation was completed is presented in b-iii.

Figure-5: (a) SEM image of magnetite FIB lamella L1 fixed on a two post copper TEM grid showing the low angle grain boundary (LAGB-1; marked by white arrow). "*M*" on bottom left marks the position where the tungsten needle was glued with platinum to lamella L1 during excavation. The image is in the XZ reference frame. Inset: IPF map of the ROI within the magnetite grain that contains the LAGB-1. (b) Bright field image of LAGB-1 that is marked by arrow in (a). Box in (b) demarcates the area for which HRTEM images are presented in Fig. 6.

Figure-6: (a) HRTEM image of LAGB-1 from the boxed area shown in Fig. 5b. LAGB-1 is marked by stripes; dashed box demarcates the striped region of LAGB-1 that is further analysed in Fig. 7. Boxes marked (b) and (c) on either side of LAGB-1 enclose the area for which Fourier transformation (FT) images were prepared. (b) and (c) are the respective FT images prepared using Inorganic Crystal Structure Database (ICSD 26410) with miller indices for cubic (spinel-type) Fe_3O_4 in [114] zone axis. FT for the same miller indices and zone axis for (a) is presented in (d). Note the presence of double reflection in (d). (e) is the magnified image of the double reflection, which is caused by rotation at the grain boundary. Rotation angles of 4.9° (α) and 4.2° (β) are determined at $(2\bar{2}0)$ and $(1\bar{3}1)$, respectively.

Figure-7: (a) High magnification HRTEM image of the striped region at the magnetite LAGB-1 that was enclosed in the dashed box in Fig. 6a. (b) Inverse Fourier Transformation (IFT) of the HRTEM image in (a) coupled with Bragg filtering using $(\bar{2}20)$ and $(2\bar{2}0)$. Note the presence of several defects (dislocations) in these lattice planes, which causes stripes at the LAGB-1. Inset in (b) is the magnified Bragg filtered image of the boxed area showing dislocation. The calculated dislocation density (ρ) in the vicinity of LAGB-1, is of the order of 10^{-1} dislocations/nm^2. See supplementary data-1 and text for details.

Figure-8: (a) SEM image of magnetite FIB lamella L2 fixed on a copper TEM grid. "*M*" on bottom left marks the position where the tungsten needle was glued with platinum to lamella L2 during excavation. The two dark spots are micro-holes that developed during FIB thinning. The image is in the XZ reference frame. Lamella L2 was extracted from the ROI that contains LAGB's with < 6° misorientation (see Fig. 3 and section 3 for description). The IPF map prepared from EBSD data of the ROI containing LAGB-2,3 is shown in the inset. (b) Bright field TEM image of the lamella L2 with [001] zone axis. The lamella contains subgrain boundaries of different orientations viz. LAGB-2 and LAGB-3. Some inclusions of another phase, marked "*I*", occur at these LAGB's. (c) and (d) are TEM images showing curvilinear geometry of magnetite subgrain boundaries in FIB lamella L2 taken in bright field with [001] and [112] zone axis, respectively. White and black triangles, respectively, mark LAGB-2 and

LAGB-3 in (c) and (d). Long white arrows in (c) and (d), respectively, point to areas of HRTEM images shown in Supplementary data-3 (SD3) and Supplementary data-4 (SD4). Note the presence of bending contours (as loop-like broad lines) in b-d that stem from the local bending of the thin lamella during the thinning process.

Figure-9: Schematic diagrams (a-c) documenting the relation between orientation of LAGB trace in the XZ reference frame of the FIB lamellae, shear strain and dislocation density. θ = angle between the grain boundary trace and X direction; ψ = angular shear; $\gamma = \tan \psi$ = shear strain; ρ = dislocation density with unit dislocations/square nanometer (dis/nm^2). (a) represents the LAGB-1 in Lamella L1, while (b) and (c) represent LAGB-2 and LAGB-3 in Lamella L2. Inset in (a) is the kernel average misorientation (KAM) map of magnetite marking the areas from where the FIB lamellae L1 and L2 (white arrows) were excavated (compare with Fig. 3a-c). (d) Schematic diagram showing a field foliation curving into a zone of strain localization (shear zone). The shear strain (γ) increases towards the zone of strain localization, as the angle between the foliation and the shear zone decreases; this is analogous to increase in shear strain (γ) for the LAGB's in magnetite, as the angle θ reduces.

Figure 10: Microstructure simulation and numerical modelling of halite polycrystals following Gomez-Rivas et al. (2017). (a) EBSD crystal orientation map of initial microstructure. EBSD crystal orientation maps of simulations performed on the latter at shear strain $\gamma = 1$, without recovery (i.e., only viscoplastic deformation) and with recovery, are shown in (b) and (c), respectively (see simulations SGC0 and SGC10 from Gomez-Rivas et al., 2017). The trace of the shear plane is horizontal and the shear sense is dextral. The addition of recovery reduces the internal misorientation (Gomez-Rivas et al., 2017), thus reducing the formation of LAGB. 6 grains are selected for a more detailed analysis (from A-F), and their dislocation density maps

are shown in Supplementary data-5. (d) and (e) are graphs of the measured dislocation density in halite across the LAGB and the angle between the LAGB and X direction (θ_H) for the 6 selected grains in the simulations with no-recovery and with recovery, respectively. Note that the dislocation density in the numerical simulations tends to increase as θ_H reduces, which is similar to the inference from TEM data of magnetite in the BIF sample (Fig. 9).

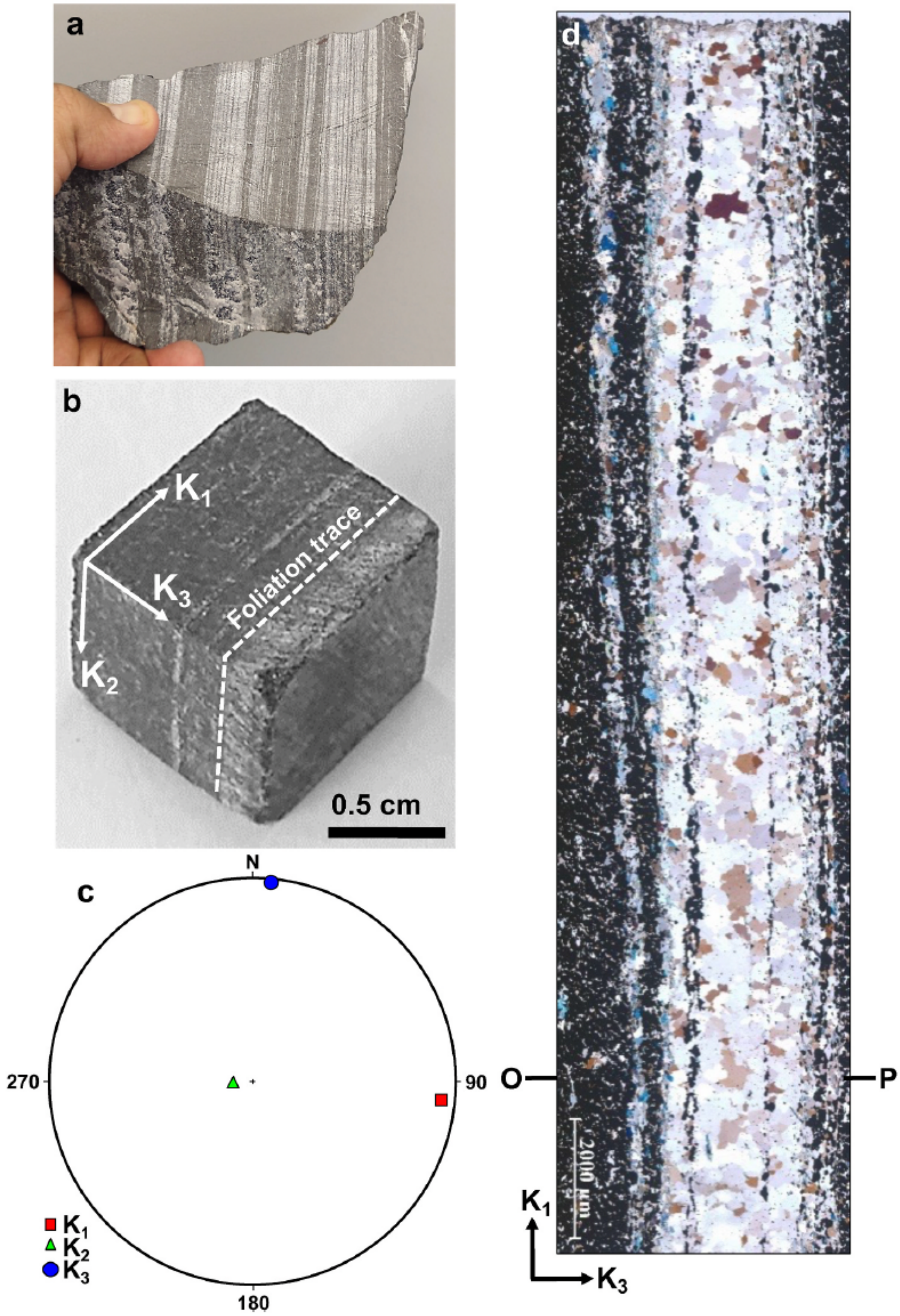
a
b
K1
K3
K2
Foliation trace
0.5 cm
c
N
270
90
180
K1
K2
K3
d
O
P
2000 μm
K1
K3

Figure 1

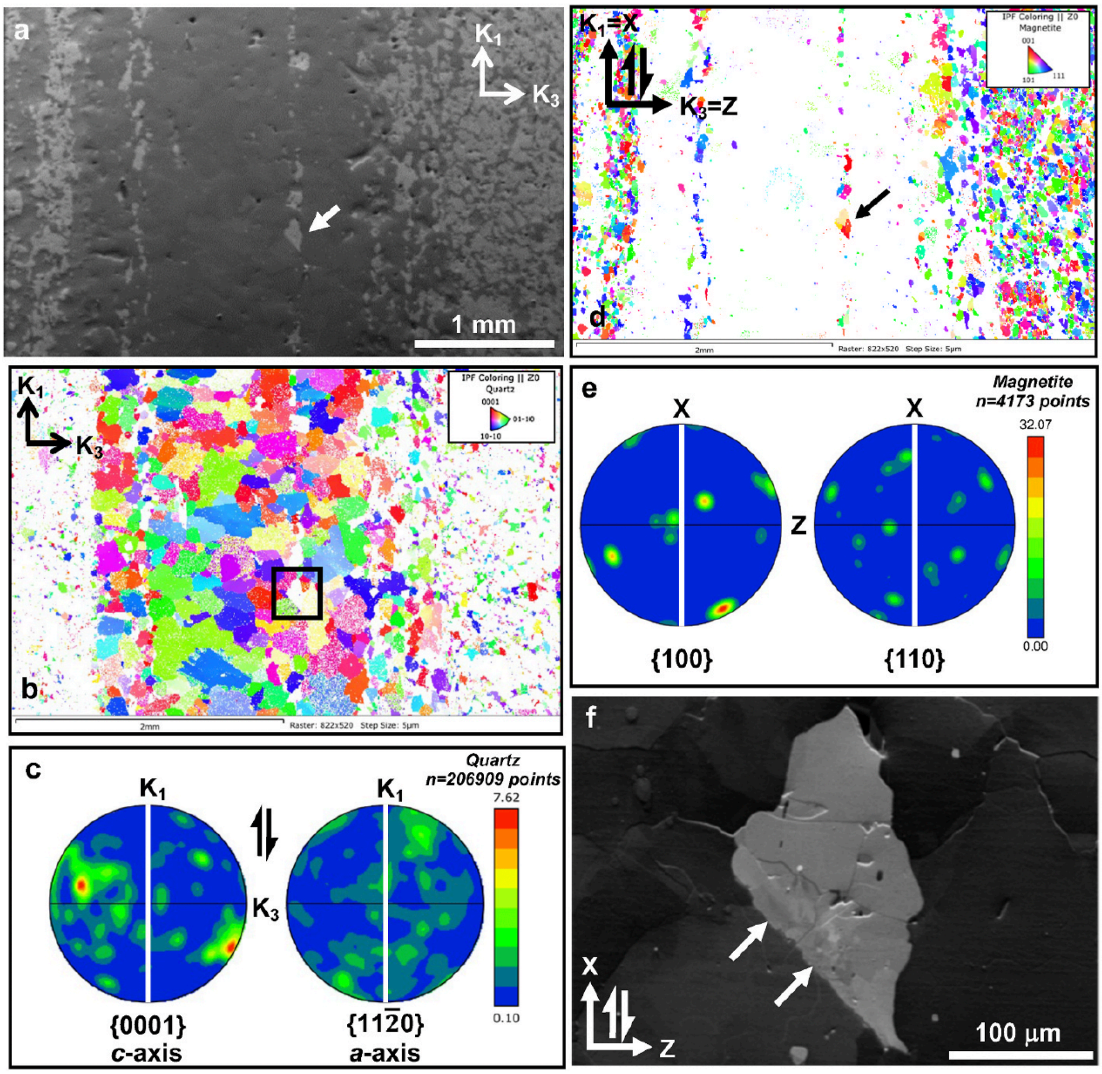

a
K1
K3
1 mm
d
K1=X
K3=Z
IPF Coloring || Z0
Magnetite
2mm
Raster: 822x520 Step Size: 5µm
b
K1
K3
IPF Coloring || Z0
Quartz
2mm
Raster: 822x520 Step Size: 5µm
e
Magnetite
n=4173 points
X
Z
32.07
0.00
{100}
{110}
c
Quartz
n=206909 points
K1
K3
7.62
0.10
{0001}
c-axis
{11$\bar{2}$0}
a-axis
f
X
Z
100 µm

Figure 2

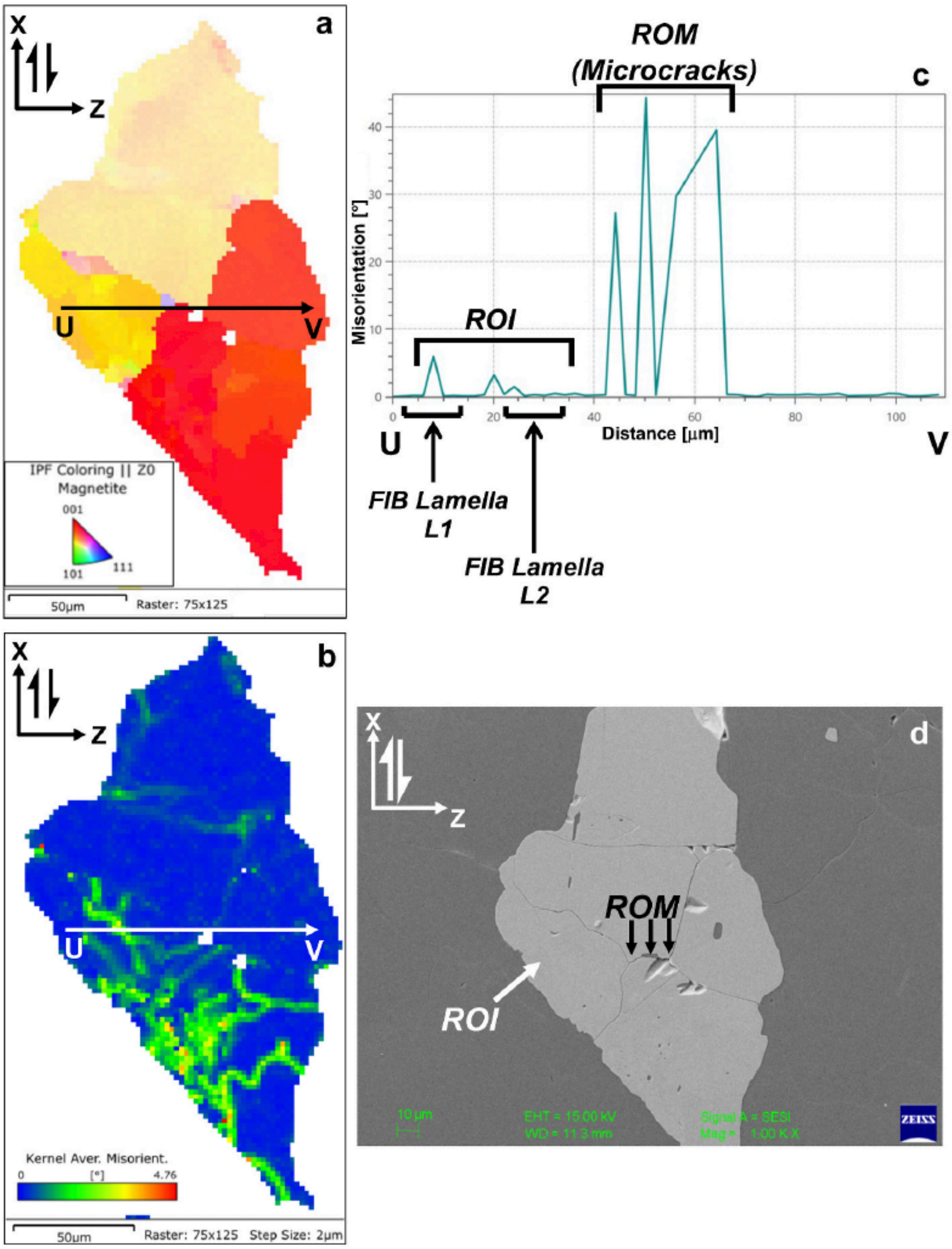
X
Z
a
U
V
IPF Coloring || Z0
Magnetite
001
101
111
50µm
Raster: 75x125
ROM
(Microcracks)
c
ROI
Misorientation [°]
Distance [µm]
U
V
FIB Lamella
L1
FIB Lamella
L2
b
Kernel Aver. Misorient.
0
[°]
4.76
50µm
Raster: 75x125
Step Size: 2µm
d
ROM
ROI
ZEISS

Figure 3

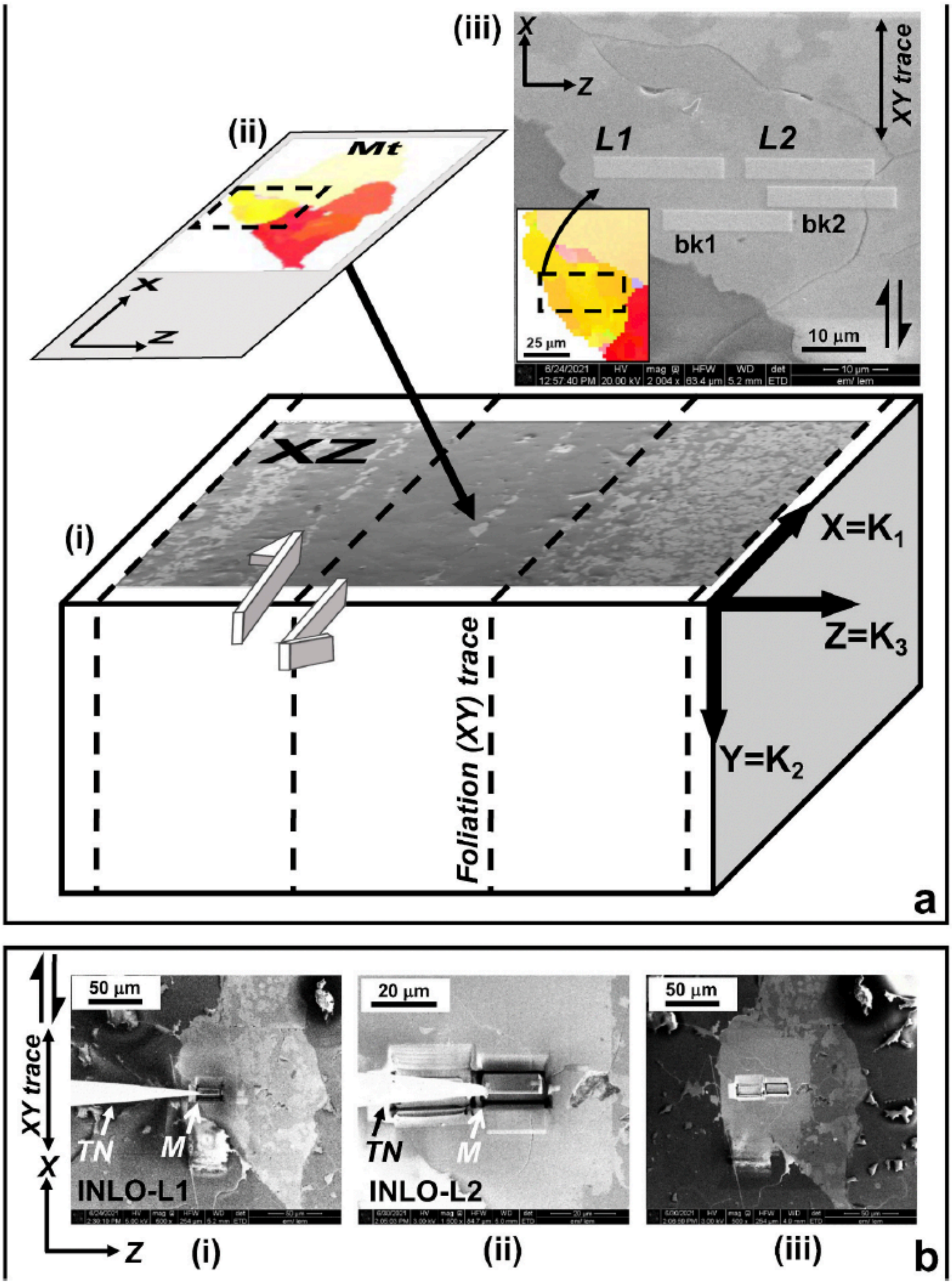
(iii)
X
Z
XY trace
L1
L2
bk1
bk2
25 µm
10 µm
(ii)
Mt
X
Z
XZ
(i)
X=K1
Z=K3
Y=K2
Foliation (XY) trace
a
50 µm
20 µm
50 µm
XY trace
TN
M
INLO-L1
INLO-L2
X
Z
(i)
(ii)
(iii)
b

Figure 4

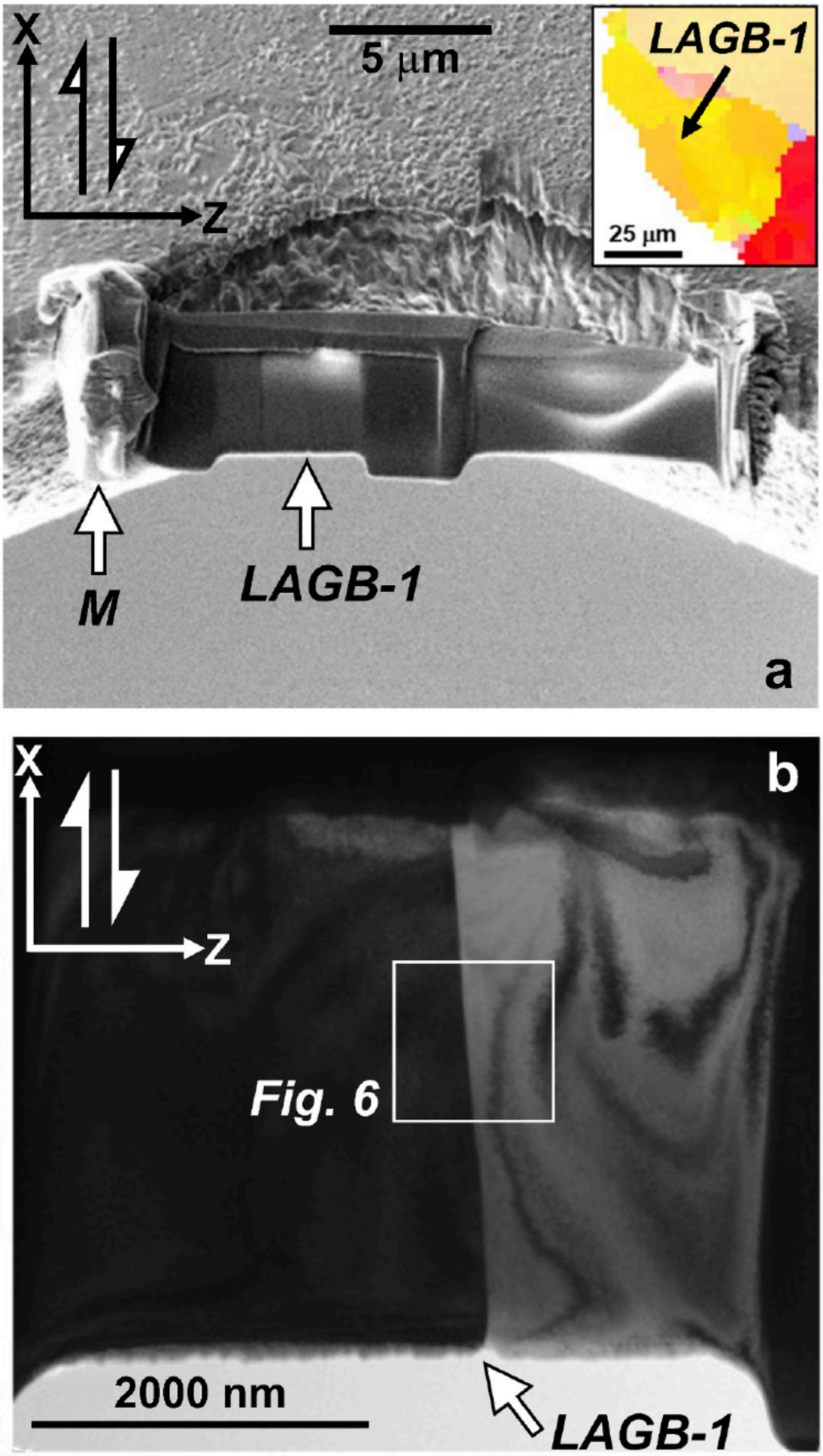

Figure 5

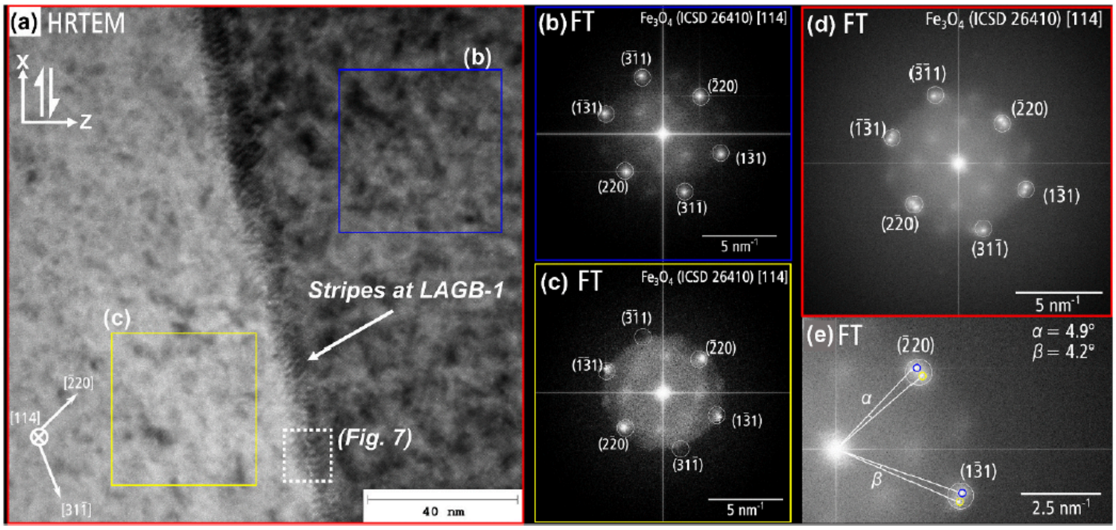

(a) HRTEM
(b)
(c)
Stripes at LAGB-1
(Fig. 7)
40 nm
(b) FT
(c) FT
(d) FT
(e) FT
Fe3O4 (ICSD 26410) [114]
5 nm-1
2.5 nm-1
α = 4.9°
β = 4.2°

Figure 6

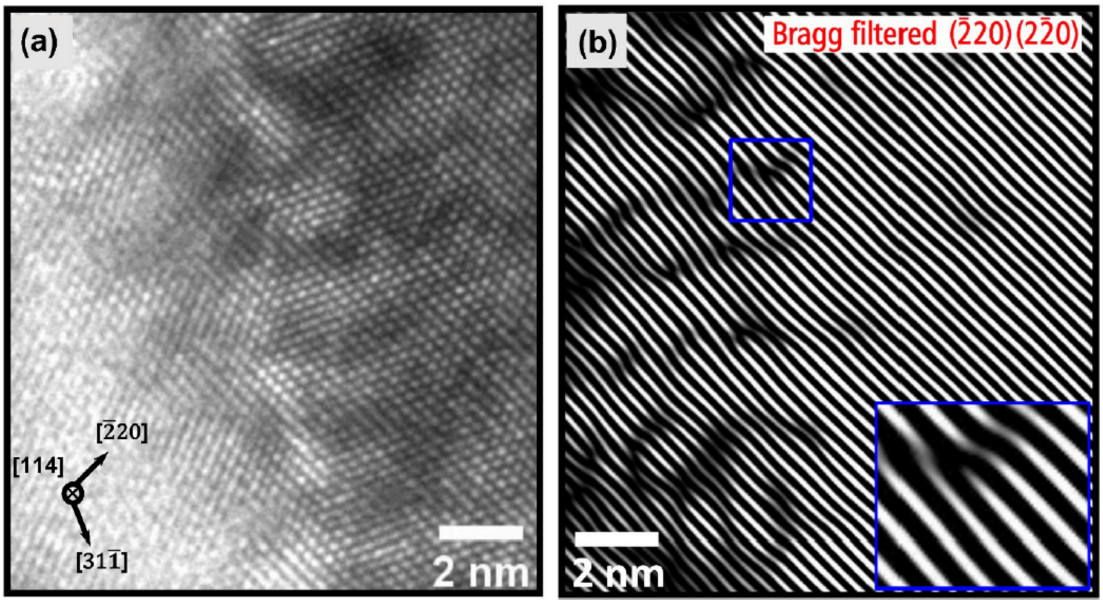

Figure 7

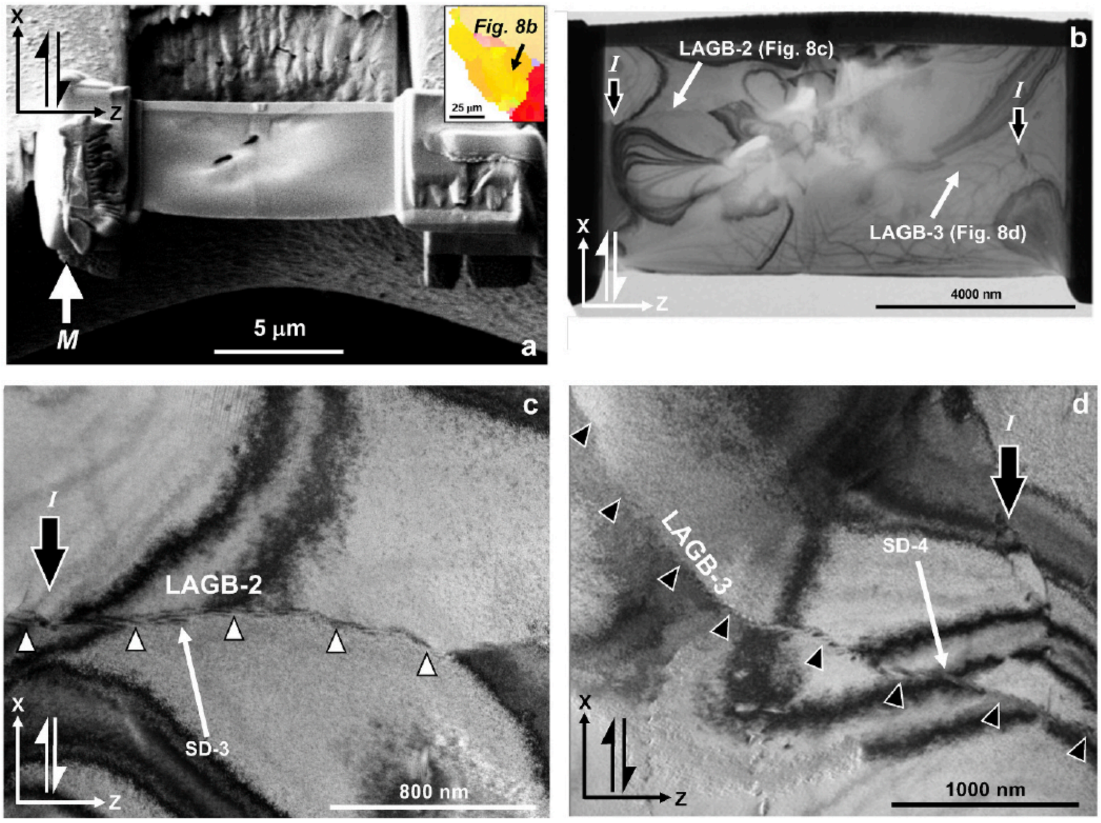
Fig. 8b
25 µm
x
z
M
5 µm
a
b
LAGB-2 (Fig. 8c)
I
I
LAGB-3 (Fig. 8d)
x
z
4000 nm
c
I
LAGB-2
SD-3
x
z
800 nm
d
I
LAGB-3
SD-4
x
z
1000 nm

Figure 8

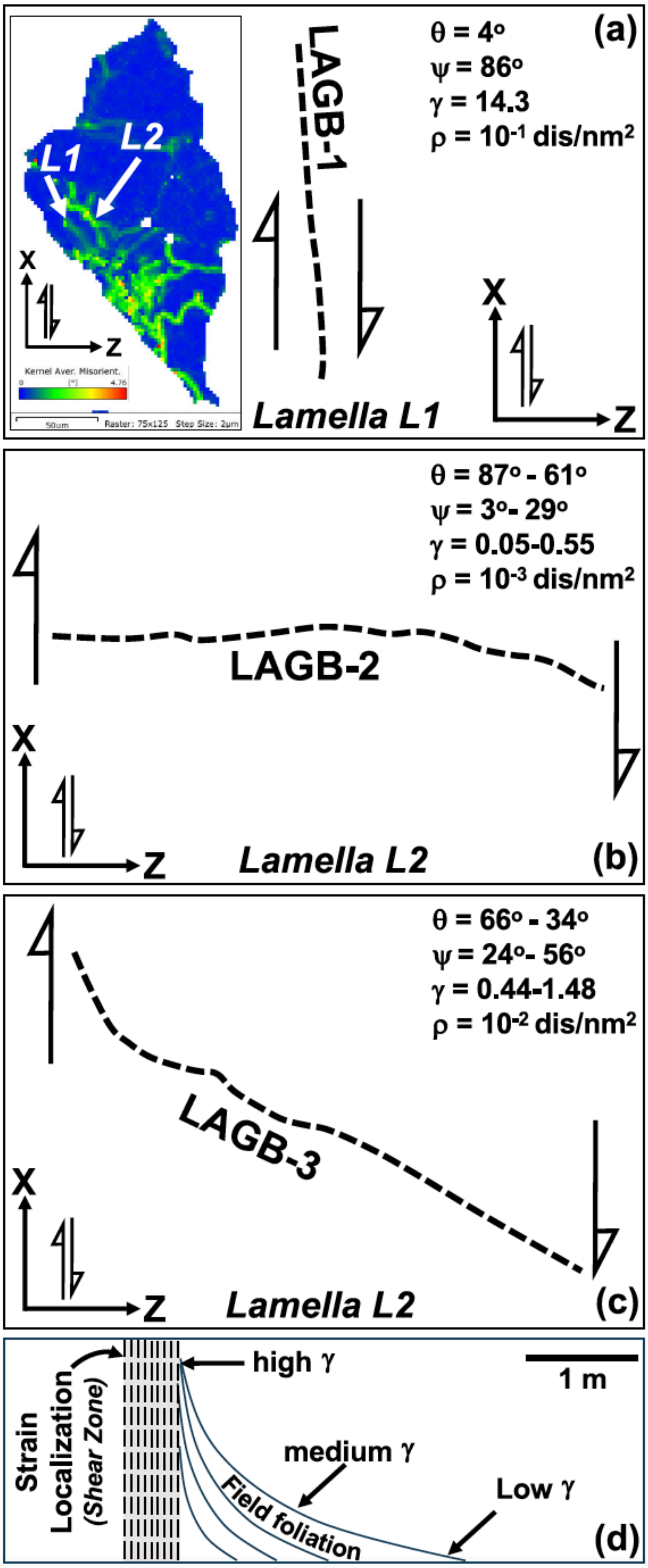
L1
L2
X
Z
Kernel Aver. Misorient.
LAGB-1
θ = 4°
ψ = 86°
γ = 14.3
ρ = 10-1 dis/nm2
(a)
Lamella L1
X
Z
θ = 87° - 61°
ψ = 3°- 29°
γ = 0.05-0.55
ρ = 10-3 dis/nm2
LAGB-2
X
Z
Lamella L2
(b)
θ = 66° - 34°
ψ = 24°- 56°
γ = 0.44-1.48
ρ = 10-2 dis/nm2
LAGB-3
X
Z
Lamella L2
(c)
Strain Localization
(Shear Zone)
high γ
1 m
medium γ
Field foliation
Low γ
(d)

Figure 9

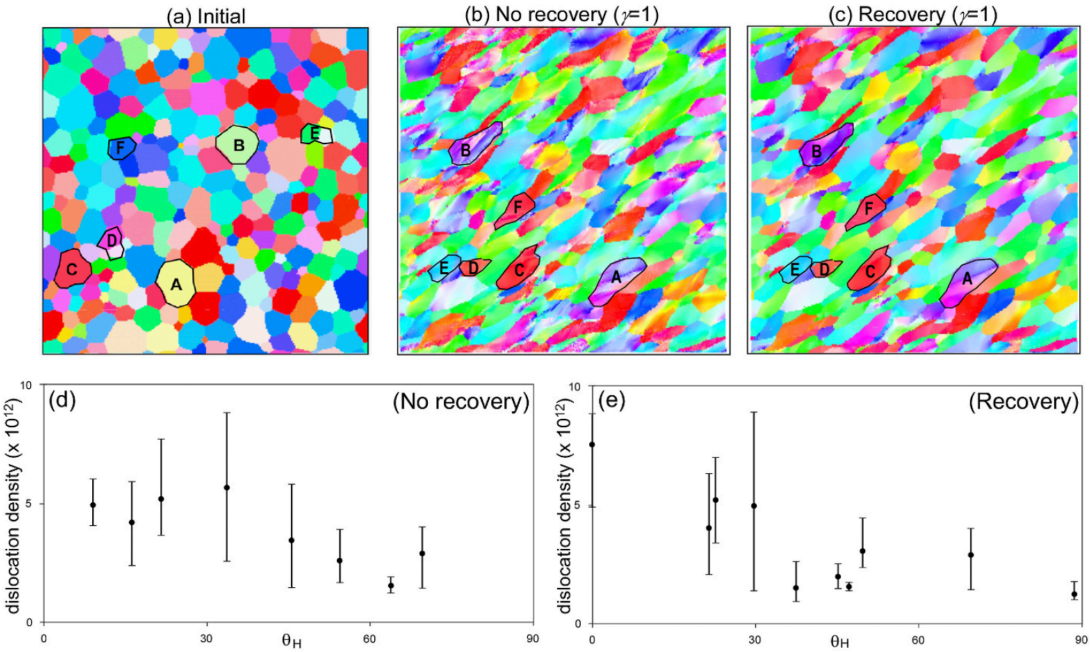

(a) Initial
(b) No recovery (γ=1)
(c) Recovery (γ=1)
A
B
C
D
E
F
(d)
(No recovery)
(e)
(Recovery)
dislocation density (x 10^{12})
θ_H
0
5
10
30
60
90

Figure 10